

# Water and cation ordering in nanocolloidal amorphous silica systems

## Part II

S. Jenkins and S.R. Kirk,  
*Dept. of Technology, Mathematics & CS,*  
*University West, P.O. Box 957, Trollhättan, SE 461 29, Sweden.*

M. Persson and J. Carlen,  
*R&D Pulp and Paper, Eka Chemicals (Akzo Nobel) AB, Rollsbo, Sweden.*

### **Abstract:**

Explicit molecular dynamics simulations were applied to two pairs of amorphous silica nanoparticles in aqueous solution (2.0 and 4.4 nm in diameter) and four different background electrolyte concentrations, to extract the potential of mean force acting between the two pairs of silica nanoparticles. Dependences of the interparticle potential of mean forces with separation and the background electrolyte concentration for the two sizes of particle radius were demonstrated. Radial distribution functions and derived quantities were used to probe the surface environment of the nanoparticles. Direct evidence of the solvation forces is presented in terms of changes of the water ordering at the surfaces of the isolated and double nanoparticles. The nature of the interaction of the counterions with charged silica surface sites (deprotonated silanols) was investigated in terms of quantifying the effects of the number of water molecules separately inside the each of the pair of nanoparticles by defining an impermeability measure. Differences in the impermeability between the pairs of nanoparticles are attributed to differences in the calculated dipole moment. A direct correlation was found between impermeability (related to the silica surface 'hairiness') and the disruption of water ordering.

## Introduction

Silica in colloidal form [1] has been used in industrial applications and studied for many decades, both in terms of production techniques [2, 3] and customization of properties. In recent years there has been a rapid increase in the number of technological applications of silica in colloidal form. In addition to the more traditional range of applications (e.g. in the food, paint, coatings, and paper industries), new ranges of applications in, e.g. the biomedical industries [4, 5] have been developed. In addition, grafted polymeric species on nanocolloidal silica enhance dispersant properties [6], silica nanoparticles can be used as hosts and carriers for other smaller, possibly toxic, particulates [7], and silica nanocolloids also form the basis for the production of zeolites [8, 9] for numerous economically important applications such as filtration and catalysis. In these applications, controlling the stability of the silica particles in (usually) aqueous solution, the size dispersion of the particles and the interactions between both the particles themselves and between the particles and other chemical species, such as solvent molecules, counterions, polyelectrolytes and other functional species, are all of prime importance. It is therefore essential that the physical and chemical phenomena underlying the production of silica colloids with desirable properties be thoroughly understood.

The Derjaguin-Landau-Verwey-Overbeek (DLVO) theory of interparticle interactions [10-12], containing terms consisting of a balance of attractive van der Waals forces and repulsive electrical double-layer forces, has been widely and successfully used to predict stability in colloidal systems. This theory, while it has long proved useful in a wide range of colloidal systems, does not account for specific ion effects [13], and neglects short- and long-ranged contributions (e.g. dispersion forces [14]) to the interparticle force which are important in some systems. Colloidal silica is such a system, and "non-DLVO" forces in silica colloids have also been attributed to additional solvation forces [15, 16] and a "hairy" nanoparticle surface [17, 18], among others [19, 20]. Additionally, DLVO theory does not provide correct predictions of stability and aggregation of silica particles up to sub-micrometer sizes in high background salt and/or low pH environments [21, 22].

Theoretical models for property prediction have been developed covering a wide range of length and time scales, Ab-initio studies of nucleation [23, 24] and stability of oligomers [25-28] have been carried out; molecular dynamics using reactive potentials has also been used in similar studies [29-32]. In recent years, some multiscale studies on silica systems have also been carried out [33-35]. A number of mesoscale approaches to colloidal structure and dynamics such as Monte-Carlo, Brownian dynamics etc. [36-41] have been in use for a much longer time - these necessarily neglect atomic-level details in order to allow longer simulated length and time scales.

The purpose of this study is to further investigate structural effects (water ordering near, and water penetration into, the silica surface), hydration and the effects of a number of experimental parameters on the effective interparticle potential acting between amorphous silica nanocolloidal particles in aqueous solution, by means of explicit molecular dynamics simulations. In particular, these effects are investigated and compared for two different sizes of nanoparticles.

## METHODS

### Modelling of amorphous silica particle structure

An amorphous silica 'starting' particle (approximately spherical, diameter 84 Å, containing 3784 atoms) was created [42] by melting, then quenching a sample of  $\alpha$ -quartz within a simulation performed using the DMol3 code [43]. Approximately spherical smaller particles were then created from copies of the 'starting' particle by removing all atoms which lay outside progressively smaller spheres [6] each sphere centered on the 'starting' particle geometrical center, the surface of each

'raw' smaller particle then being repaired and all resultant surface hydroxyl groups reconstructed. The set of progressively smaller test particles generated in this way were equilibrated at 300K before later use.

### Allocation of surface charge on silica test particles

Negative partial charges were allocated to the test silica particles by deprotonating surface hydroxyl (Si-OH  $\rightarrow$  Si-O<sup>-</sup>) groups, and assigning an additional -1 partial charge to the deprotonated oxygen. The number of deprotonated sites was determined by the experimental Si:Na ratio used in the industrial production process (usually in the range 10:1-40:1; for this work we chose a value for the ratio of 20:1). The number of silicon atoms in each particle then determined the number of residual sodium atoms. The number of surface hydroxyl groups to be deprotonated was then set equal to the number of residual Na<sup>+</sup> ions, for overall charge neutrality. Deprotonation sites on each test particle were allocated using a Monte Carlo optimization algorithm, taking account of the mutual repulsion of the deprotonated sites. The position coordinates of all surface hydroxyl oxygen atoms were recorded, then a subset of size  $N$  of these sites chosen at random. The sum  $S$  over the  $N$  sites of  $|\mathbf{r}_{ij}|^{-2}$ , where  $\mathbf{r}_{ij}$  is the position vector between sites  $i$  and  $j$ , was then calculated (avoiding the double sum) for the current subset. One site is then chosen randomly from the subset, swapped with a random site not currently in the subset, and  $S$  recalculated. If  $S$  increases as a result of the swap, the swap is allowed, otherwise the swap is rejected. This process is repeated over many steps, with the subset of sites evolving towards the 'maximally repulsive' configuration. The simple form used for the 'fitness function'  $S$  was chosen for computational efficiency, and to allow for the surface roughness and non-sphericity of the silica particles.

### Molecular dynamics

Molecular dynamics calculations were carried out in the NVT ensemble using the GROMACS [44-46] code (version 3.3.1), using OPLS-AA [47] force fields, with additional parameters for silica from literature [48]. The water model used was a flexible variant of the TIP4P 4-site model [49, 50]. During actual MD runs, the simulation temperature of all species was set to 300K, particle velocities being chosen from a Maxwell distribution, using a Berendsen [51] thermostat with a coupling time constant of 0.1 ps. Neighbour list, Coulomb and van der Waals cutoffs were all set to 1 nm. Centre of mass motion was removed after every timestep. Long-range electrostatic forces were treated using a particle-mesh Ewald [52] treatment, with long-range dispersion corrections applied. The FFT grid spacing was in all cases around 0.118 nm, varying slightly with simulation box size, and cubic (order 4) spline interpolation was used on the FFT grid. In all cases, a 3-stage MD protocol was used - energy minimization, followed by 100 ps (0.002 ps timestep) of position-restrained MD, followed by the 'production' run (performed with 0.001 ps timestep). In cases where a non-zero background salt concentration was modelled, an appropriate number of water molecules in the simulation box were randomly substituted with equal numbers of Na<sup>+</sup> and Cl<sup>-</sup> ions to reach the desired concentration.

### Single-particle MD runs

The test nanoparticles were centered in cubic simulation boxes with periodic boundary conditions; the boxes were then filled with water, the box size being chosen so that there was at least 1 nm of water between any side of the box and the nanoparticle, in order to avoid potential spurious water structuring effects caused by the periodicity of the simulation box [53]. Sodium ions were substituted in randomly for water molecules until the contents of the simulation box was overall electrically neutral. The production run in these cases consisted of a 500 ps unconstrained MD run, all other parameters being as previously stated.

## Double-particle MD runs - PMF calculations

The fully equilibrated test nanoparticles from the single-particle MD runs were used as building blocks to investigate interparticle interactions. Pairs of nanoparticles (along with their accompanying cloud of neutralizing  $\text{Na}^+$  ions) were placed relative to each other in such a way that the distance between their centres of mass (COM distance) took a number of specified values. The resulting nanoparticle pairs were then centered in large simulation boxes with periodic boundary conditions applied. The dimensions of these large simulation boxes were chosen such that the any part of one nanoparticle was closer to all parts of the other member of the pair than to any periodic copies of either particle. The remaining space in the simulation boxes was filled with TIP4P water. In these runs the production phase consisted of a 500 ps (0.001 ps timestep) potential of mean force (PMF) calculation, using the constraints method built into the pull code within GROMACS. The COM distance between the nanoparticle pair at the end of the position-restrained MD run was used as a constraint distance. An additional constraint force was applied by the GROMACS code during the PMF production run to maintain this original COM distance, and the value of the constraint force needed to maintain this distance was monitored and recorded at every timestep of the production run. After the end of the production run, the 500,000 values of these constraint forces were averaged, representing the average interparticle attractive or repulsive force caused by interactions between the particles [54]. Variants of these basic PMF runs were generated and carried out for various different background concentrations of NaCl in the solvent (the additional ions having been present from the beginning of the protocol), in the form of additional  $\text{Na}^+$  and  $\text{Cl}^-$  ions randomly substituted for solvent (water) molecules. Numbers of additional ions were chosen to replicate molecular background salt concentrations of 0.00M, 0.01M, 0.1M and 1.0M, encompassing the range of background salt levels used in industrial production of these nanoparticles, and found in their common applications.

## Results and discussion

In Figure 1(a) and (b) we show the calculated potential of mean forces (PMF) for two sizes of particles (2.0 nm and 4.4 nm in diameter) used in this study, by integration of the mean interparticle forces (details can be found in Part I of this study). We removed the constant of integration by estimating the potential at infinite range (i.e. zero) to be the value at the largest range used in our calculations. In general, we observed that the multiple simulation runs started with initial COM distance values chosen with a constant increment (0.5 nm) yielded constraint distances for the PMF phase of the simulation runs (i.e. after the preliminary temperature equilibration position-restraints phase) which did not have a constant spacing, as can be seen from Figure 1(a) and (b), under the influence of the oscillatory interparticle forces. It can be seen from Figure 1(a) that the PMF for the smaller silica nanoparticle pair is rather more attractive than that of the larger one. This may explain why the pairs of 2.0 nm diameter particle on occasion 'crashed' (see later in this section) i.e. had a large attractive force and small (approximately 0.2 nm) final separation during the PMF phase of the calculations. This behaviour was not observed in the larger silica nanoparticles. Notice that in Figure 1(b) the form of a depletion well and a repulsive structural barrier stabilizer [55] can be seen; this barrier contributes in preventing the large particles from flocculating or coalescing.

The hydrogen bond length (hydrogen-acceptor oxygen) distributions between water molecules (see Figure 12(a)) was determined from the PMF MD trajectories, the peak in the distribution being found at 0.18 nm across all of the simulations for particles of different sizes: this compares well with the experimentally determined hydrogen bond length in water [56]. The distribution of hydrogen bond lengths between nanoparticles and water molecules is shown in Figure 2(b); the position of the first peak being found at 0.15 nm and the second at 0.25 nm. From Figure 2(c), the peak in the length distribution of the hydrogen bonding between the surface oxygen sites  $\text{O}^-$  and water molecules was located at a distance of 0.15 nm; this shows the hydrogen bonds are rather

short due to the excess charge at the oxygen surface site. Note also that this peak coincides with the first peak in Figure 2(b).

In order to quantify the spatial effects of the various background concentrations of  $\text{Na}^+$  on the surface and beyond we have calculated a set of three radial distribution functions (*rdfs*); the *rdfs* for water around the sodium ions and the deprotonated oxygen surface sites ( $\text{O}^-$ ) and for the sodium ions around the deprotonated oxygen surface sites ( $\text{O}^-$ ), shown in Figures 3(a-c) respectively. Examining the figures in more detail reveals some important details about the nature of the surface of the silica nanoparticles. In Figure 3(b) the first peak is at a distance of 0.15 nm from the  $\text{O}^-$  site, the second at 0.24 nm. When this is compared with Figure 3(c), where the first peak is at 0.23 nm and the second is at 0.35 nm, it is apparent that the water molecules are closer to the  $\text{O}^-$  surface site than are the sodium ions. Figure 3(b) also reflects the results of the hydrogen bonding distributions in Figure 2(b). Another interesting feature is the fact that in both Figure 3(a) and (b) the *rdf* after the first peak is close to zero. This is more similar to the typical *rdf* of a solid rather than a liquid, showing as it does some ordering or layering effects in the water around the surface of the nanoparticles.

In Tables 1-2 a summary of the *rdf* data is presented for the two sizes of silica nanoparticles considered in this study, listing both the pairwise interaction of same sized nanoparticles and the isolated nanoparticle for comparison. Examining the first set of entries ( $\text{Na}^+$  and  $\text{H}_2\text{O}$ ) in Tables 1 and 2 it can be seen that there is a monotonic increase of the height ratio (second peak to first) with background sodium concentration. This variable is used to quantify the extent to which the second species is 'piling up' around the first species used in the analysis. This holds true for both the double particles and isolated particles. Closer inspection shows that the *rdf* entry ( $\text{Na}^+$  and  $\text{H}_2\text{O}$ ) for the double particle in Table 1 is almost identical to that of the double particle in Table 2, the same relation holding for the isolated particles. The change in the  $\text{Na}^+$  and  $\text{H}_2\text{O}$  *rdf* ratio with increasing background sodium concentration could be explained in terms of the sodium ions binding the water and preventing it from entering the nanoparticle.

The time-averaged number of water molecules found within the nanoparticles was extracted from the PMF MD trajectories (as shown in Figure 4), and the mean values of these numbers across all investigated interparticle separations listed in Tables 3 and 4. Table 3 shows that as the background sodium concentration increases, the amount of water entering the nanoparticle with diameter 2.0 nm decreases. This relationship is less simple for the larger nanoparticle (see Table 4), as the instance of 0.00M background sodium doesn't correspond to the largest number of water molecules entering the nanoparticle, which could be due to the much larger surface density of charged surface sites, and hence associated sodium counterions on the larger nanoparticle. In addition, the isolated particle case in Table 4 has more water molecules entering the larger nanoparticle in all background sodium concentrations as compared with any of the sodium background concentrations for the double nanoparticle case. This is evidence that the sodium double layer of counterions is acting more strongly in the double particle of the 4.4 nm nanoparticles, as seen by the fewer sodiums entering each of the pair of the double particle systems (see Table 4).

Differences between the double particle and isolated particle for the smaller particles are again evident from Table 3, the converse being true this time, i.e. there are fewer water molecules entering the isolated 2.0 nm diameter nanoparticle than the double nanoparticle. This can be explained by the existence of only 5 deprotonated surface  $\text{O}^-$  sites positioned approximately equatorially on the silica particle, the number of these sites being determined by the experimental Si:Na ratio as explained earlier. The double layer formed around the pair of nanoparticles is apparently sufficiently strong to attract the water molecules to the surface of the pair of nanoparticles, but more 'leaky' towards the influx of water molecules than the isolated nanoparticle. It is evident that the double layer of sodium counterions formed in the case of the nanoparticle with

diameter 2.0 nm is sufficient to attract water molecules, as shown in Figures 5(a-b) (where the plots of variation of the number of water molecules with background sodium concentration within 0.5 nm of the O<sup>-</sup> surface) are similar to those of the (4.4 nm) nanoparticle which are shown in Figure 5 (c-d).

The solvation forces (also referred to as hydration forces for water) do not occur because the water molecules have formed semi-ordered layers at the surface, but rather because of the disruption of the ordering due to the approach of a second surface [57]. This can be seen if we compare the orientation plot (as shown in Figure 6(a) and 6(b) - the definition of the orientation can be found in the Figure caption) of the water molecules around the isolated particle and the double particle respectively. Notice in particular the difference in these Figures (see accompanying figure captions also) in the vicinity of 2 nm. From Tables 3 and 4, it can be seen that the impermeability (defined as the dry core radius of a nanoparticle measured radially from the centre of mass of the nanoparticle, in nanometres) of the nanoparticle with diameter 2.0 nm is higher generally than that of the larger nanoparticle. This shows that the larger (4.4 nm diameter) nanoparticle is 'hairier' than the smaller nanoparticle. This observation has important consequences for explaining the lack of regular oscillatory behaviour of the mean force vs. separation plots for the larger particle relative to the smaller one. It is worth noting that the level of 'hairiness' can be controlled within an industrial setting. The increased 'hairiness' of the 4.4 nm nanoparticle, demonstrated by the low values of the impermeability, will disrupt the water ordering at the surface and hence disrupt the oscillatory form of the forces. The reduction in water ordering is seen by inspection of Figures 7(a-b) which show the axial-radial density plot of the distribution of water molecules around the pairs of nanoparticles for the entire MD trajectory, for the nanoparticles with diameter 2.0 and 4.4 nm respectively. The relative size and apparent extent of water layering is greater in Figure 7(a) and for that of the larger nanoparticle in Figure 6(b).

In Table 1 for the entry O<sup>-</sup> and H<sub>2</sub>O, notice in particular that for the isolated particle the *rdf* ratios for 0.00M and 1.00 M background Na<sup>+</sup> are nearly identical. This is not the case for the double particle. This pattern also occurs in the larger nanoparticle for O<sup>-</sup> and H<sub>2</sub>O; see Table 2. For the final *rdf* ratio, that is O<sup>-</sup> and Na<sup>+</sup> in Tables 2 and 3, there are large differences between the 2.0 and 4.4 nm nanoparticles, since in the case of the larger nanoparticles the *rdf* ratios are much smaller and the double particle and isolated particle cases have similar values for a given background sodium concentration. The small values of the O<sup>-</sup> and Na<sup>+</sup> *rdf* ratios show that the sodium ions are rather more confined around the silica nanoparticles, i.e. at the first peak in the *rdf*.

In Table 3 the impermeability shows that the water molecules penetrate significantly into the nanoparticles with diameter 2.0 nm in all cases. In the isolated particle, the water molecules don't penetrate as far in 3 out of the 4 background sodium concentrations, 0.00M, 0.01M and 1.00M, as is the case for the double particle. In Table 3 the results for a 'bare' particle (i.e. all the silanol surface sites are protonated), are also presented. The bare particles are always softer (i.e. have lower values of the impermeability) than the isolated or double particles for a given sodium background concentration. Failures in analysis software prevented the corresponding result for the larger nanoparticle being evaluated.

In Table 4, clearer differences emerge; for the double particle case, nanoparticle 1 (denoted 'snp 1') has a higher value of the impermeability than nanoparticle 2 (denoted 'snp 2') for all investigated values of the background sodium concentration. In addition, the isolated nanoparticle has consistently much lower values of the impermeability than either of the nanoparticles in the double particle case. This is consistent with the isolated nanoparticle having more water molecules penetrate it, and shows that the findings in this work go beyond starting geometries, i.e. since we use the same nanoparticle in both sets of calculations. In effect the isolated nanoparticle is 'softer' than either of the twin nanoparticles. This can be explained in terms of the weaker double layer of

sodium counterions in the isolated nanoparticle than in the double nanoparticle case. It can be seen that the variation of the number of water molecules inside the pair of nanoparticles doesn't vary regularly with particle separation; see Figures 4(a-h). This effect is more apparent for the 2.0 nm diameter particle (e.g. note the large spike in the result for  $\text{Na}^+$  concentration = 0.01 M) than the 4.4 nm particle, as seen by comparing Figures 4(b) and 4(f) respectively. But, as has been mentioned earlier, there are predictable trends in the number of water molecules inside the nanoparticles when time-averages are taken over all background sodium concentrations (see Tables 3 and 4). Notice that for both sizes of nanoparticle in this study, there are variations in the number of water molecules inside each of a pair of nanoparticles - a physical reason for this could be that the two particles have different dipole moments. The individual nanoparticles are distinguishable and labelled 'snp 1' and 'snp 2' in Figure 4, and have average (over separation) dipole moments of approximately 2100 and 2700 Debye for each of the 2.0 nm diameter nanoparticles respectively, and approximately 31000 and 42000 Debye for the 4.4 nm diameter nanoparticle. The value of the dipole moment is found to be independent of the molarity of the background sodium. These variations in the dipole moments could explain the differences in the number of water molecules trapped inside the two nanoparticles (see Tables 3 and 4) for a given background sodium concentration.

## Conclusions

This study, along with the accompanying Part I, has successfully modelled the interactions between, and near-surface structure of, amorphous silica nanoparticles in aqueous solutions with varying amounts of background counterions using realistic molecular dynamics force fields, evaluating the interparticle potentials using a PMF formalism. In order to investigate the dependence of a number of properties on particle size, we studied the largest and smallest of a set of sample simulated nanoparticles.

This work shows that water molecules can penetrate into amorphous silica nanocolloid particles, and that 'hairiness' of the silica surface (modelled at atomic resolution with a realistic silica surface structure) has an effect on the interparticle potential of mean force, in agreement with other work in the literature [17,18], describing a thin 'hairy' layer on the surfaces of such systems. The consequences for water ordering has also been investigated, in conjunction with the presence of surface-bound and free background counterions. The hydrogen bonding characteristics in the surface region were found to be independent of particle size, although as mentioned previously in Part I of this work, the smaller particles showed a much greater tendency to 'crash' together during the course of the simulation runs than the larger particles, resulting in the particles being directly hydrogen bonded to each other with no intervening water molecules or sodium counterions. In addition, we have quantified and examined the factors influencing the effectiveness of the sodium counterion 'double layer' in preventing or enabling water molecules entering the silica nanoparticle.

Reactive MD potentials [58] and QM/MM [59,60] treatments may provide a future avenue for investigations of the longer time-scale interactions between 'crashed' particles as condensation reactions between silanol groups create bonds as the particles 'fuse' together. At longer length and time-scales, the interparticle potentials derived in this work will inform ongoing coarse-grained MD investigations of flocculation and gelation in silica nanocolloid systems, with the eventual goal of creating a microscopic theory of gelation in partnership with novel application of mathematical network formalism to utilize the universal structural character of colloids [61].

## Acknowledgments

Thanks go to Zareen Abbas for useful discussions. The Knowledge Foundation are gratefully acknowledged for the support of SJ and SRK, grant number 2004/0284. This work was made possible by the facilities of the Shared Hierarchical Academic Research Computing Network

(SHARCNET:[www.sharcnet.ca](http://www.sharcnet.ca)), through the kind auspices of our sponsor Dr. P.W. Ayers, Department of Chemistry, McMaster University, Ontario, Canada.

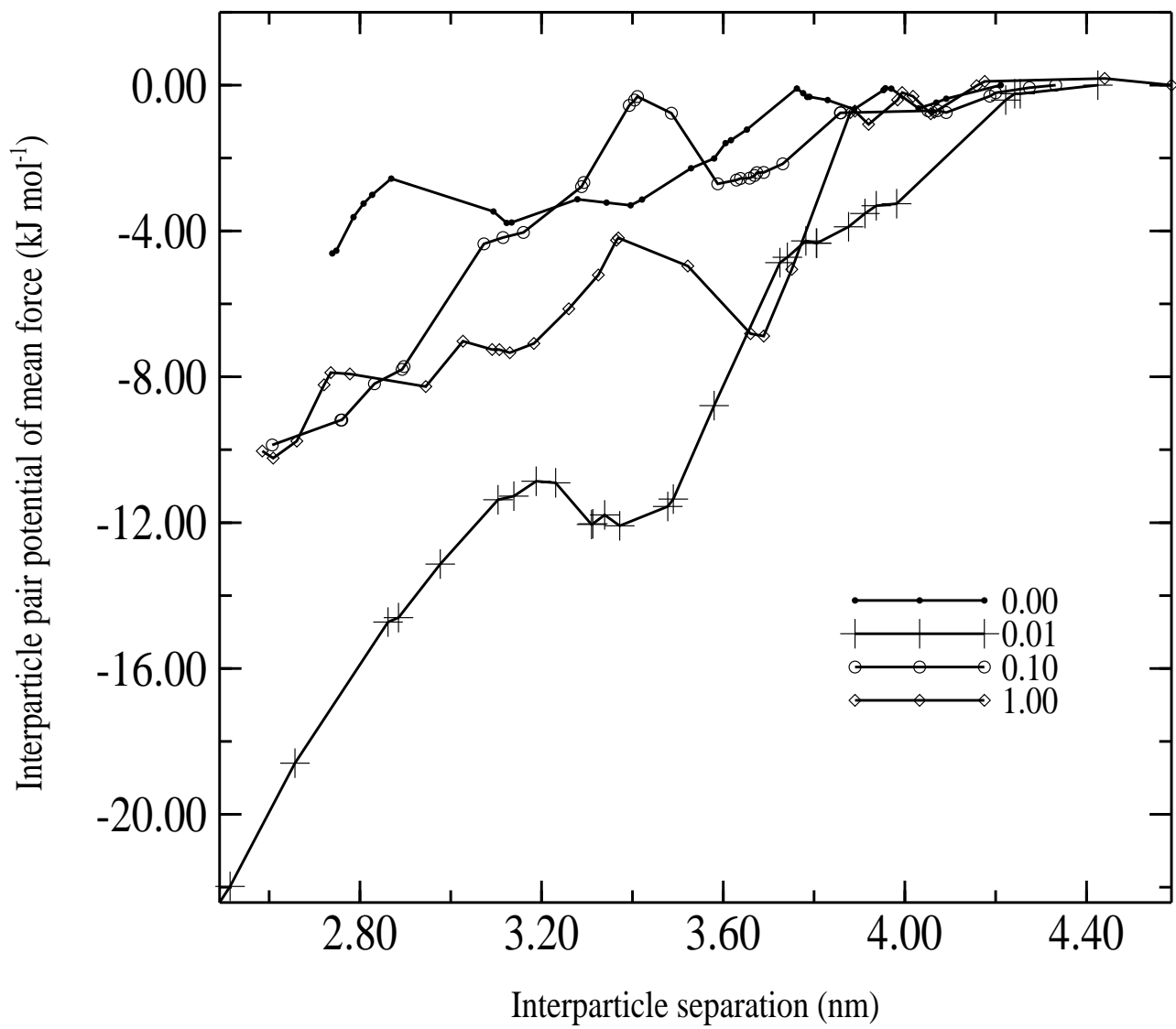
## References

- [1] R. K. Iler, *The Chemistry of Silica* (Wiley Interscience, 1979).
- [2] W. Stober, A. Fink, and E. Bohn, *Journal of Colloid and Interface Science* **26**, 62 (1968).
- [3] D. L. Green *et al.*, *Journal of Colloid and Interface Science* **266**, 346 (2003).
- [4] W. Tan, and W. Kemin, *Medicinal Research Reviews* **24**, 621 (2004).
- [5] T. Pellegrino, and K. Stefan, *Small* **1**, 48 (2005).
- [6] D. Barbier *et al.*, *Macromolecules* **37**, 4695 (2004).
- [7] C. Graf *et al.*, *Langmuir* **22**, 5604 (2006).
- [8] S. M. Auerbach, M. H. Ford, and P. A. Monson, *Current Opinion in Colloid & Interface Science* **10**, 220 (2005).
- [9] T. M. Davis *et al.*, *Nature Materials* **5**, 400 (2006).
- [10] B. V. Derjaguin, and L. Landau, *Acta Physicochim. URSS* **14**, 108 (1941).
- [11] B. V. Derjaguin, and L. D. Landau, *Zh. Eksp. Teor. Fiz* **15**, 663 (1945).
- [12] E. J. W. Verwey, and J. T. C. Overbeek, *Theory of the Stability of Lyophobic Colloids* (Dover, 1999).
- [13] M. Bostrom, D. R. M. Williams, and B. W. Ninham, *Physical Review Letters* **87**, 168103 (2001).
- [14] S. A. Edwards, and D. R. M. Williams, *Physical Review Letters* **92**, 248303 (2004).
- [15] J. J. Valle-Delgado *et al.*, *Journal of Chemical Physics* **123** (2005).
- [16] S. Song *et al.*, *Journal of Colloid and Interface Science* **287**, 114 (2005).
- [17] G. Vigil *et al.*, *Journal Of Colloid And Interface Science* **165**, 367 (1994).
- [18] M. Kobayashi *et al.*, *Langmuir* **21**, 5761 (2005).
- [19] G. V. Franks, *Journal of Colloid and Interface Science* **249**, 44 (2002).
- [20] J. Depasse, and A. Watillon, *Journal of Colloid and Interface Science* **33**, 430 (1970).
- [21] L. H. Allen, and E. Matijevic, *Journal of Colloid and Interface Science* **31**, 287 (1969).
- [22] M. Kobayashi *et al.*, *Journal of Colloid and Interface Science* **292**, 139 (2005).
- [23] J. C. G. Pereira *et al.*, *Journal of Sol-Gel Science and Technology* **8**, 55 (1997).
- [24] J. C. G. Pereira, C. R. A. Catlow, and G. D. Price, *Chemical Communications*, 1387 (1998).
- [25] Y. He *et al.*, *Journal of Chemical Physics* **124** (2006).
- [26] E. Flikkema, and S. T. Bromley, *Journal of Physical Chemistry B* **108**, 9638 (2004).
- [27] J. C. G. Pereira, C. R. A. Catlow, and G. D. Price, *Journal of Physical Chemistry A* **103**, 3252 (1999).
- [28] J. C. G. Pereira, C. R. A. Catlow, and G. D. Price, *Journal of Physical Chemistry A* **103**, 3268 (1999).
- [29] N. Z. Rao, and L. D. Gelb, *Journal of Physical Chemistry B* **108**, 12418 (2004).
- [30] K. Yamahara, and K. Okazaki, *Fluid Phase Equilibria* **144**, 449 (1998).
- [31] B. P. Feuston, and S. H. Garofalini, *Chemical Physics Letters* **170**, 264 (1990).
- [32] B. P. Feuston, and S. H. Garofalini, *Journal of Physical Chemistry* **94**, 5351 (1990).
- [33] S. B. Trickey *et al.*, *Journal of Computer-Aided Materials Design* **13**, 1 (2006).
- [34] H. P. Cheng *et al.*, *Journal of Computer-Aided Materials Design* **13**, 161 (2006).
- [35] S. Joseph, and N. R. Aluru, *Langmuir* **22**, 9041 (2006).
- [36] J. Z. Wu *et al.*, *The Journal of Chemical Physics* **111**, 7084 (1999).
- [37] A. Videcoq *et al.*, *Physica A: Statistical Mechanics and its Applications* **374**, 507 (2007).
- [38] J. C. Chen, and A. S. Kim, *Advances in Colloid and Interface Science* **112**, 159 (2004).
- [39] P. Linse, *Advanced Computer Simulation Approaches For Soft Matter Sciences II* **185**,

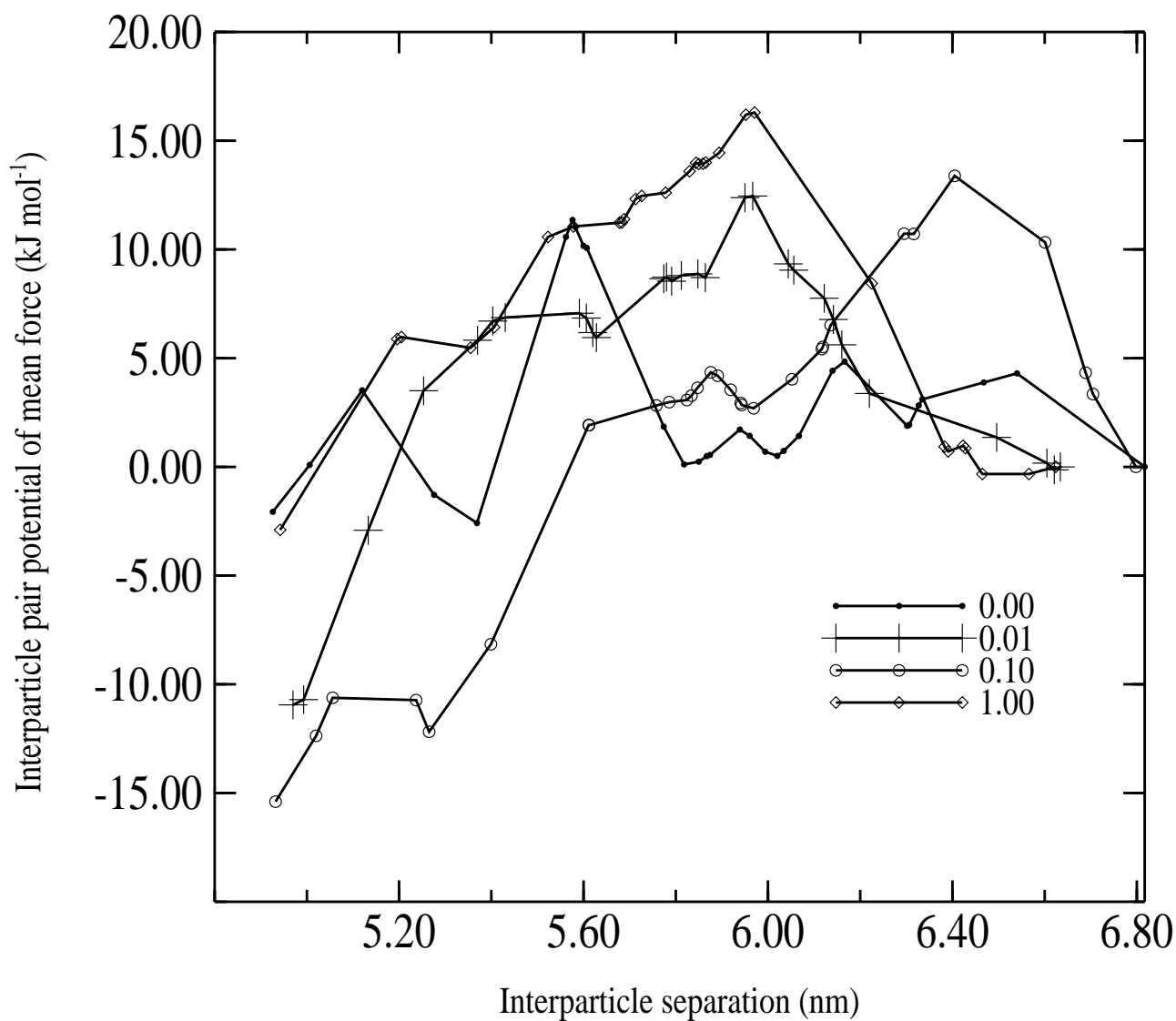


111 (2005).

- [40] M. Jonsson, M. Skepo, and P. Linse, *Journal of Physical Chemistry B* **110**, 8782 (2006).
- [41] A. Evilevitch *et al.*, *Langmuir* **17**, 1043 (2001).
- [42] I. Panas, (Chalmers University of Technology, Gothenburg, 2005).
- [43] B. Delley, *Journal of Chemical Physics* **92**, 508 (1990).
- [44] H. J. C. Berendsen, D. van der Spoel, and R. van Drunen, *Computer Physics Communications* **91**, 43 (1995).
- [45] E. Lindahl, B. Hess, and D. van der Spoel, *Journal of Molecular Modeling* **V7**, 306 (2001).
- [46] D. Van der Spoel *et al.*, *Journal of Computational Chemistry* **26**, 1701 (2005).
- [47] W. L. Jorgensen, in *Encyclopedia of Computational Chemistry* (Wiley, 1998), pp. 1986.
- [48] E. J. W. Wensink *et al.*, *Langmuir* **16**, 7392 (2000).
- [49] W. L. Jorgensen *et al.*, *The Journal of Chemical Physics* **79**, 926 (1983).
- [50] C. P. Lawrence, and J. L. Skinner, *Chemical Physics Letters* **372**, 842 (2003).
- [51] H. J. C. Berendsen *et al.*, *J. Chem. Phys.* **81**, 3684 (1984).
- [52] U. Essmann *et al.*, *The Journal of Chemical Physics* **103**, 8577 (1995).
- [53] D. Van der Spoel, and P. J. vanMaaren, *Journal of Chemical Theory and Computation* **2**, 1 (2006).
- [54] D. Trzesniak, and A.-P. E. Kunz, *ChemPhysChem* **8**, 162 (2007).
- [55] D.T Wasan, *et al.*, 'Confinement-induced structural forces in colloidal systems', *Encyclopedia of Surface and Colloid Science*, 2002 M. Dekker, Inc.
- [56] M. Hakala, *et al.*, *Journal of Chemical Physics* **125** 084504 (2006).
- [57] J.N. Israelachvili, *Intermolecular and Surface Forces: With Applications to Colloidal and Biological Systems*, (Academic Press, 1991)
- [58] S. Bhattacharaya and J. Kieffer, *Journal of Chemical Physics* **122**, 094715 (2005)
- [59] H. Lin and D.G. Truhlar, *Theoretica Chimica Acta* **117**, 185 (2007)
- [60] P.K. Biswas and V. Gogonea, *Journal of Chemical Physics* **123**, 1 (2005)
- [61] M. Y. Lin, *et al.*, *Nature* **339**, 360 (1989).

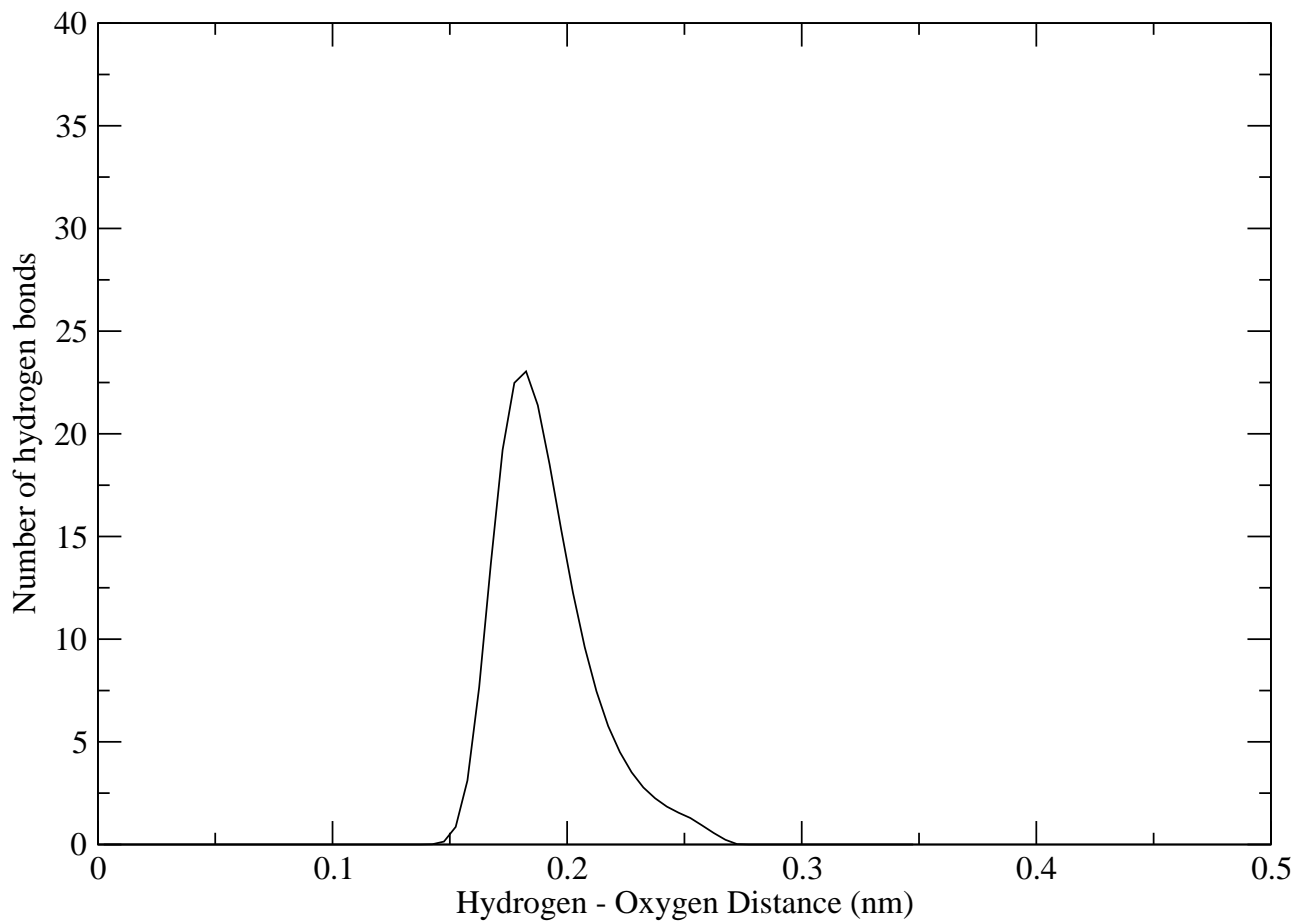


(a)

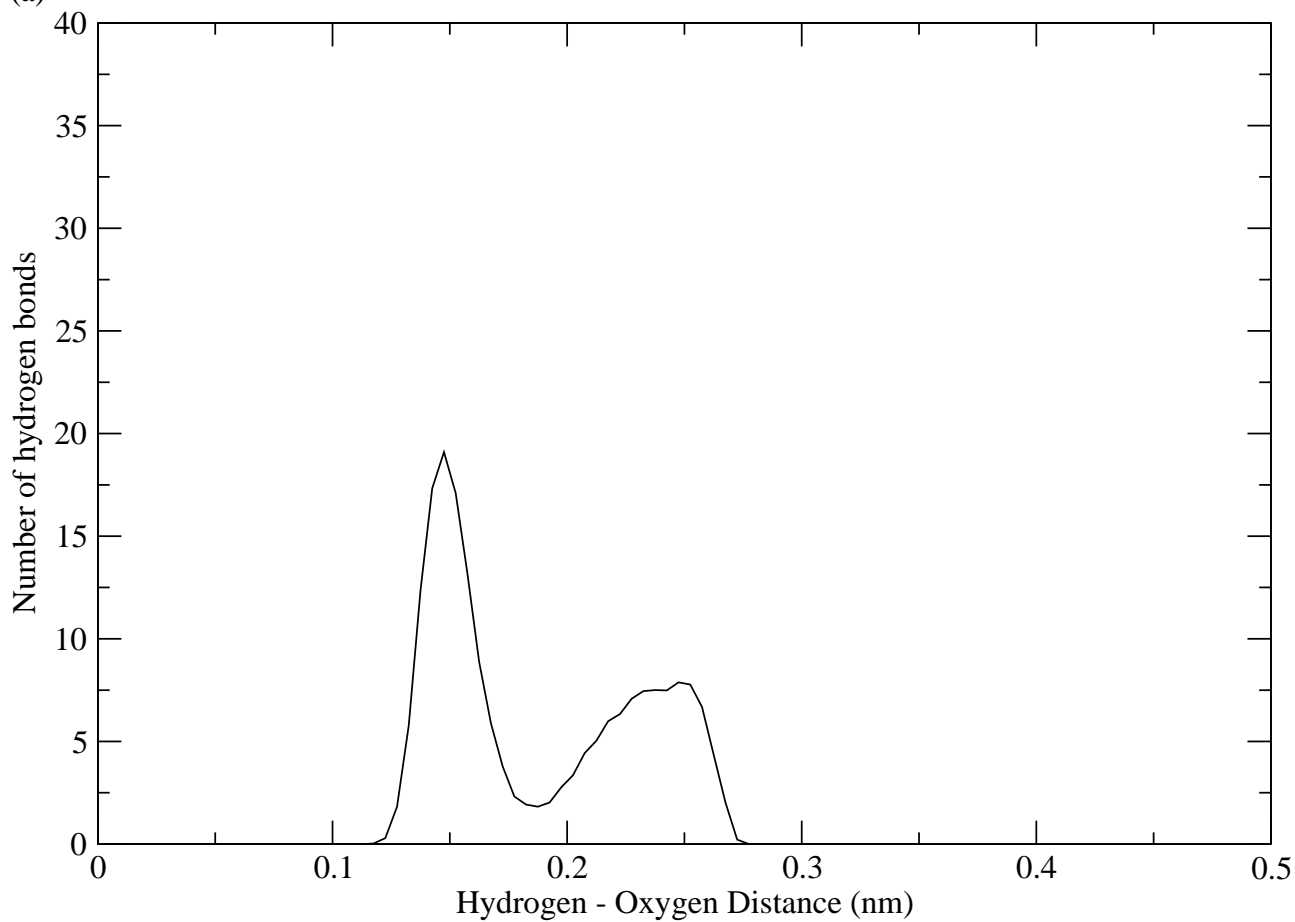


(b)

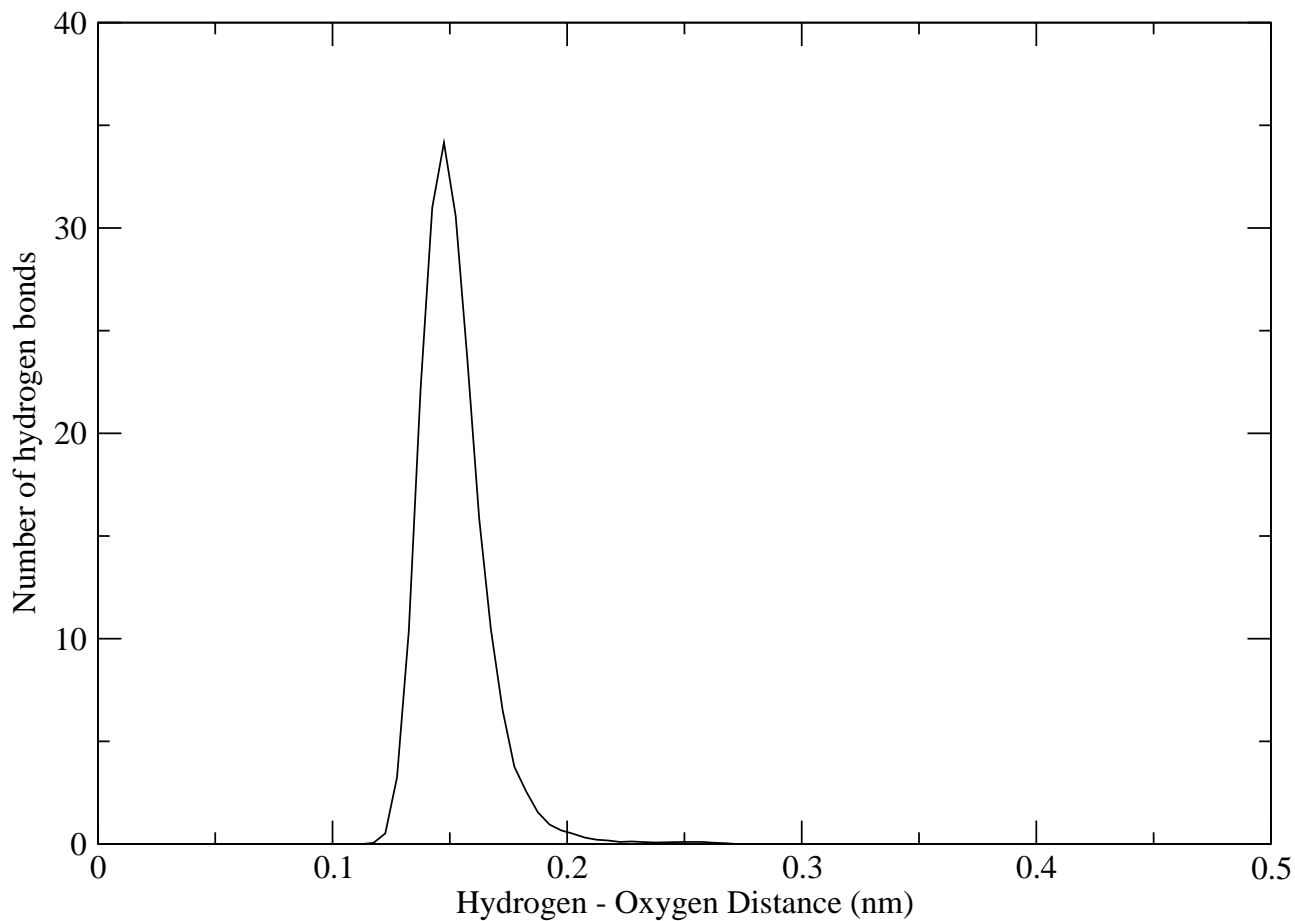
**Figure 1.** The potential of mean forces (PMF) for the two sizes of particles in this study shifted to estimate for the infinite range potential, where the PMF pair potential for the silica nanoparticle with radii 2.0 and 4.4 nm are shown in (a) and (b) respectively.



(a)

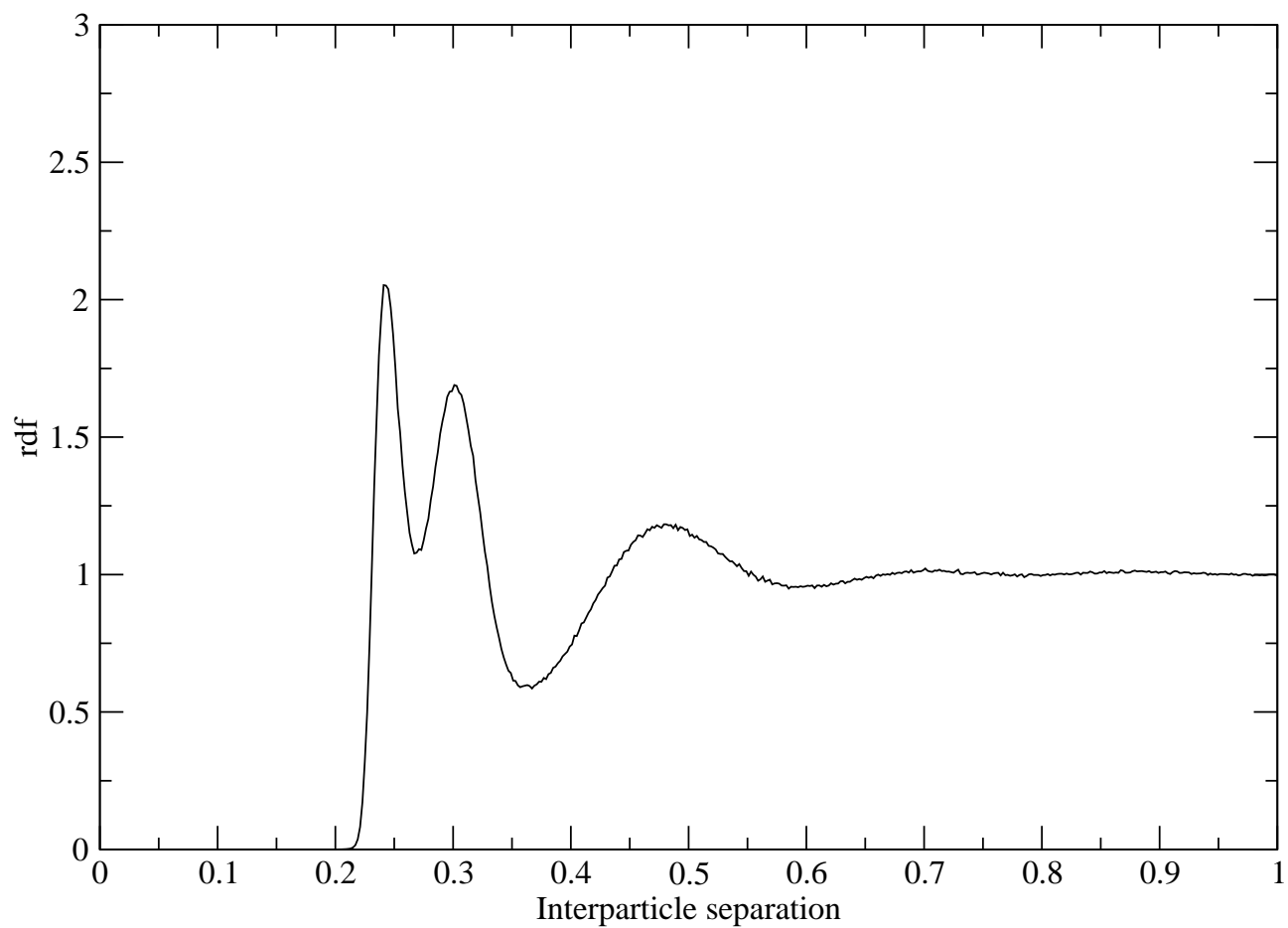


(b)

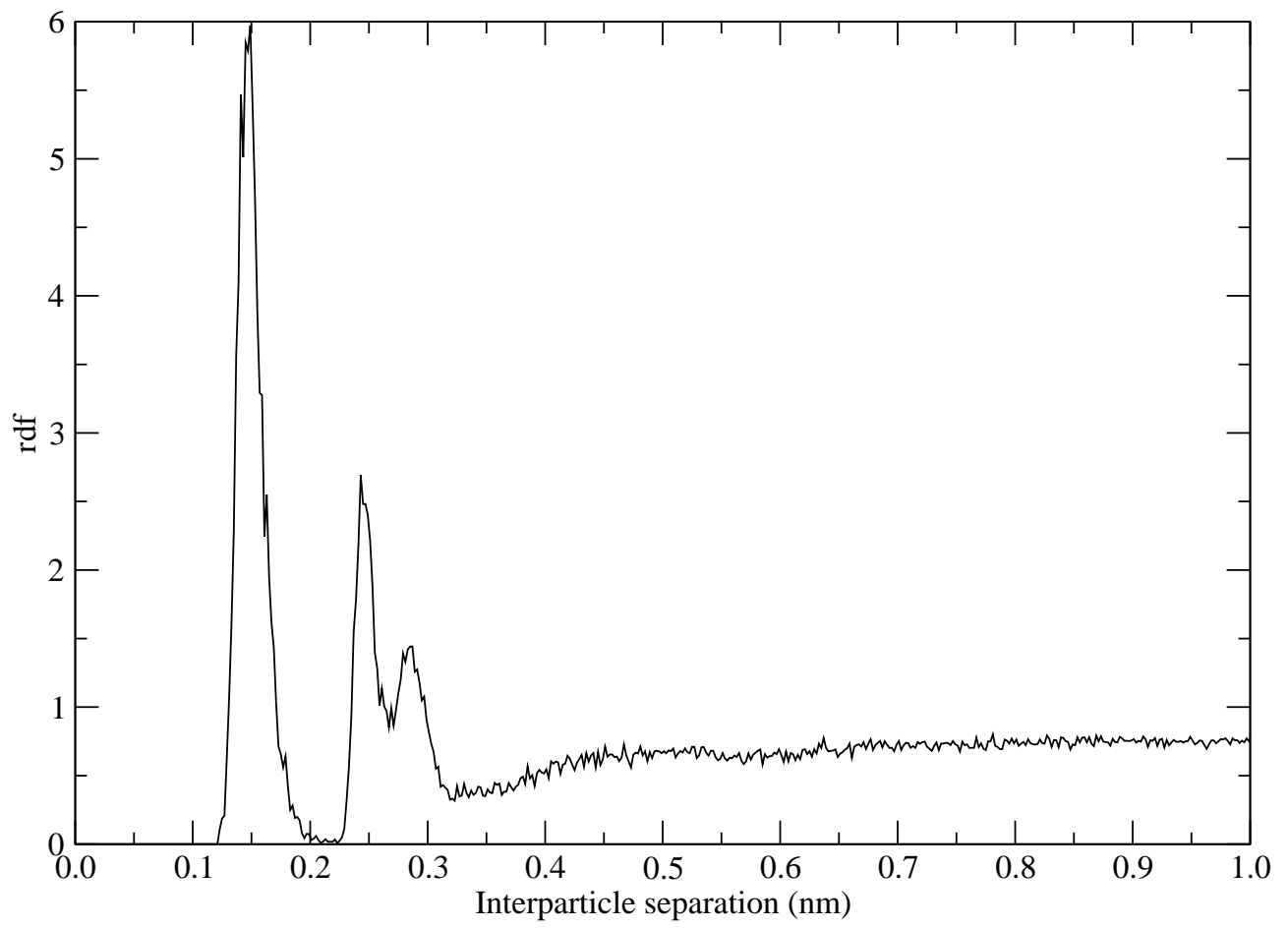


(c)

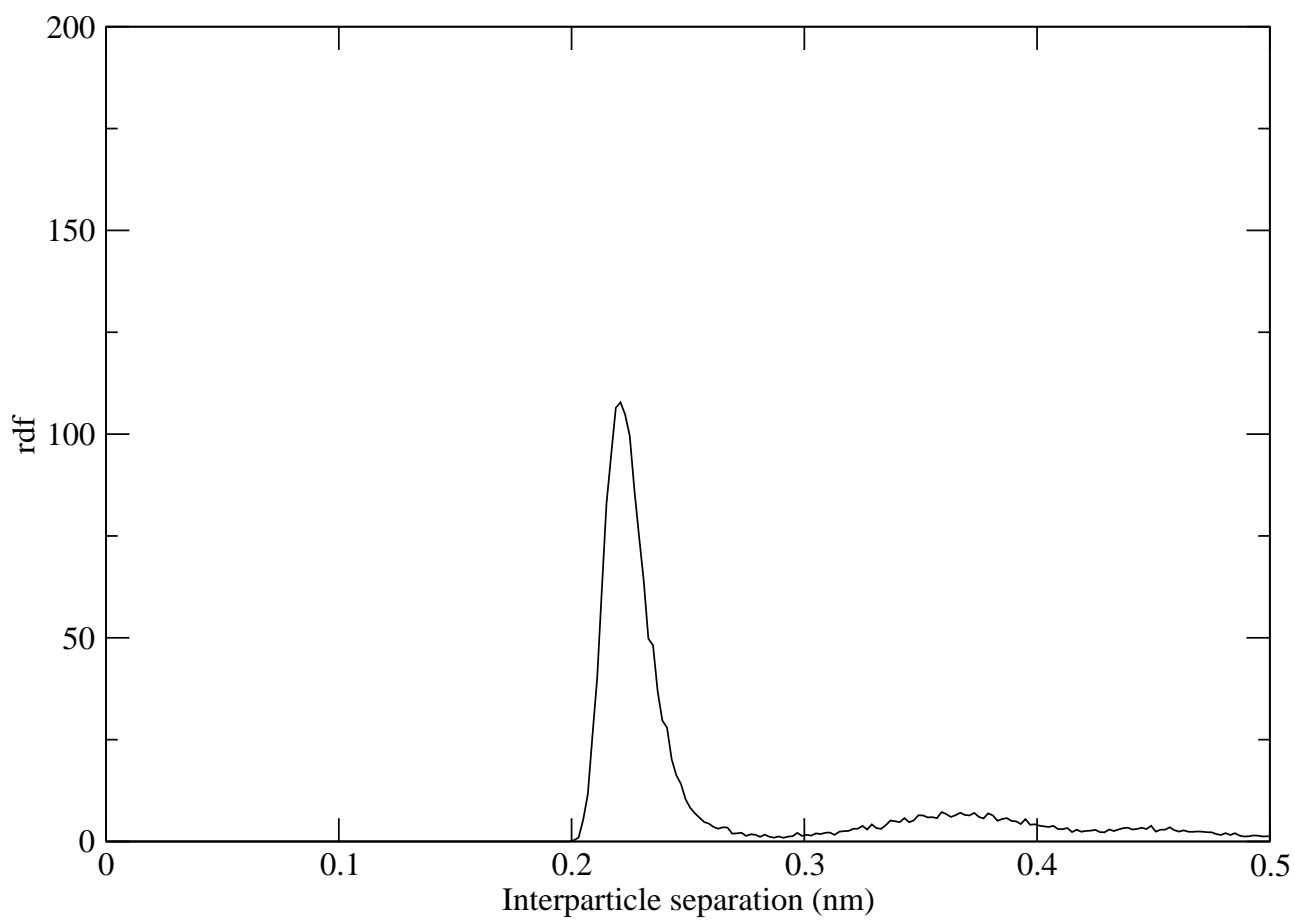
**Figure 2.** (a) The hydrogen bonding length (hydrogen-acceptor) distribution between the (flexible TIP4P) water molecules in the simulation; (b) shows the distribution of hydrogen bond lengths between nanoparticles and water molecules. The peak in the hydrogen bond length distribution of the hydrogen bonding between the surface oxygen sites O<sup>-</sup> and water molecules is given in (c).



(a)



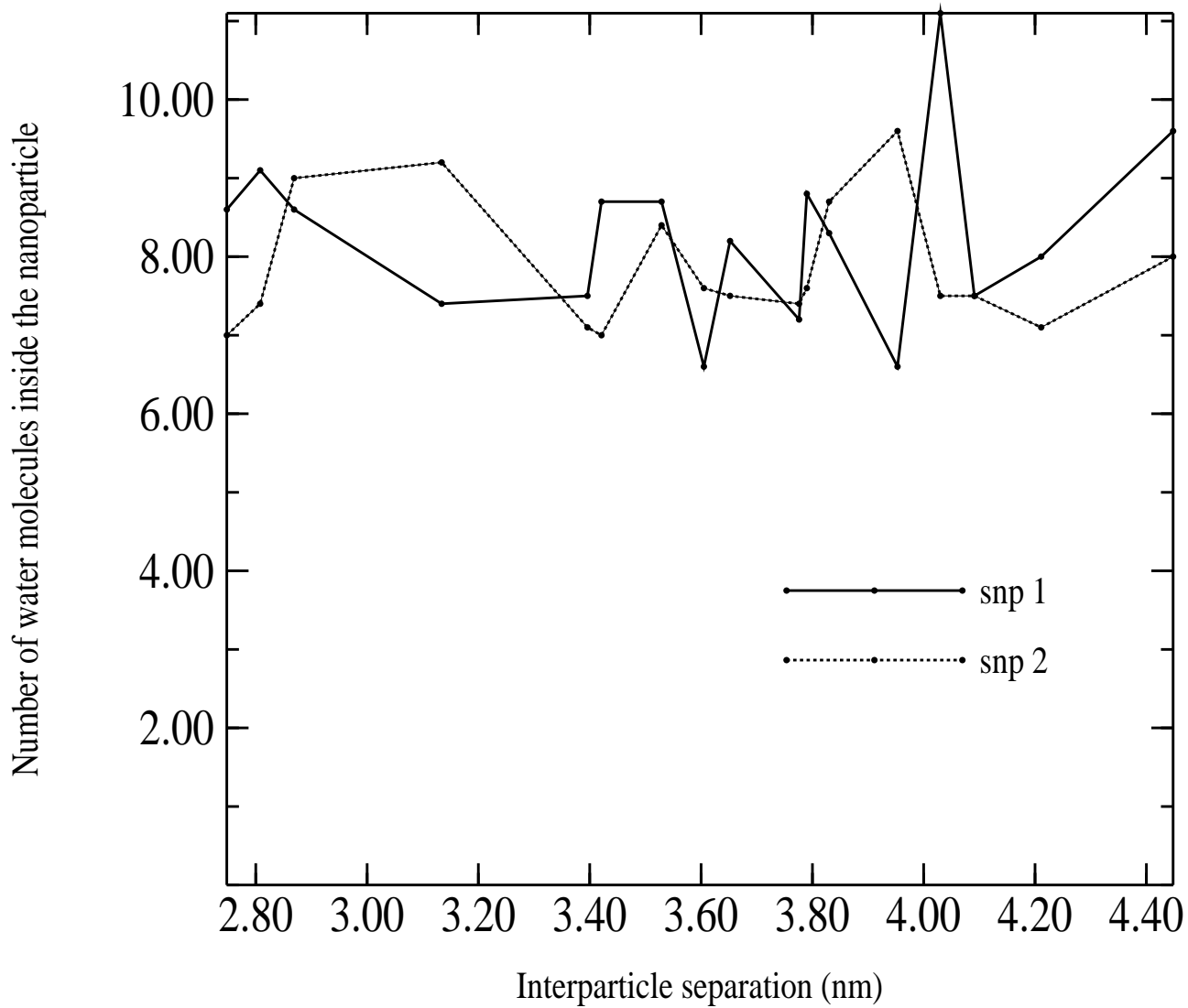
(b)



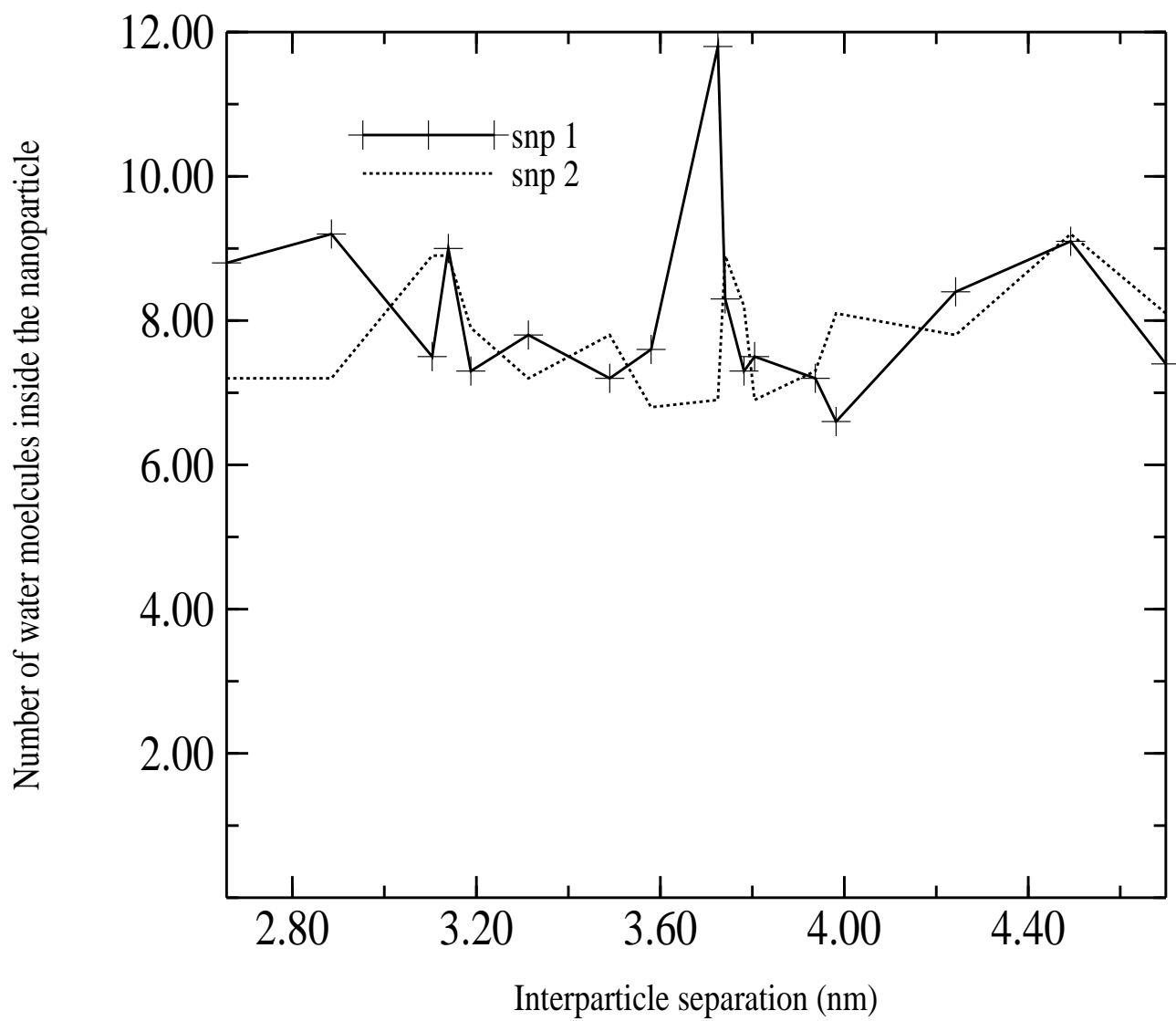
(c)

**Figure 3.** The radial distribution functions (*rdf*) for water around the sodium ions is shown in (a), water around the deprotonated oxygen surface sites ( $O^-$ ) shown in (b) and the sodium ions around the deprotonated oxygen surface sites ( $O^-$ ) is shown in (c).

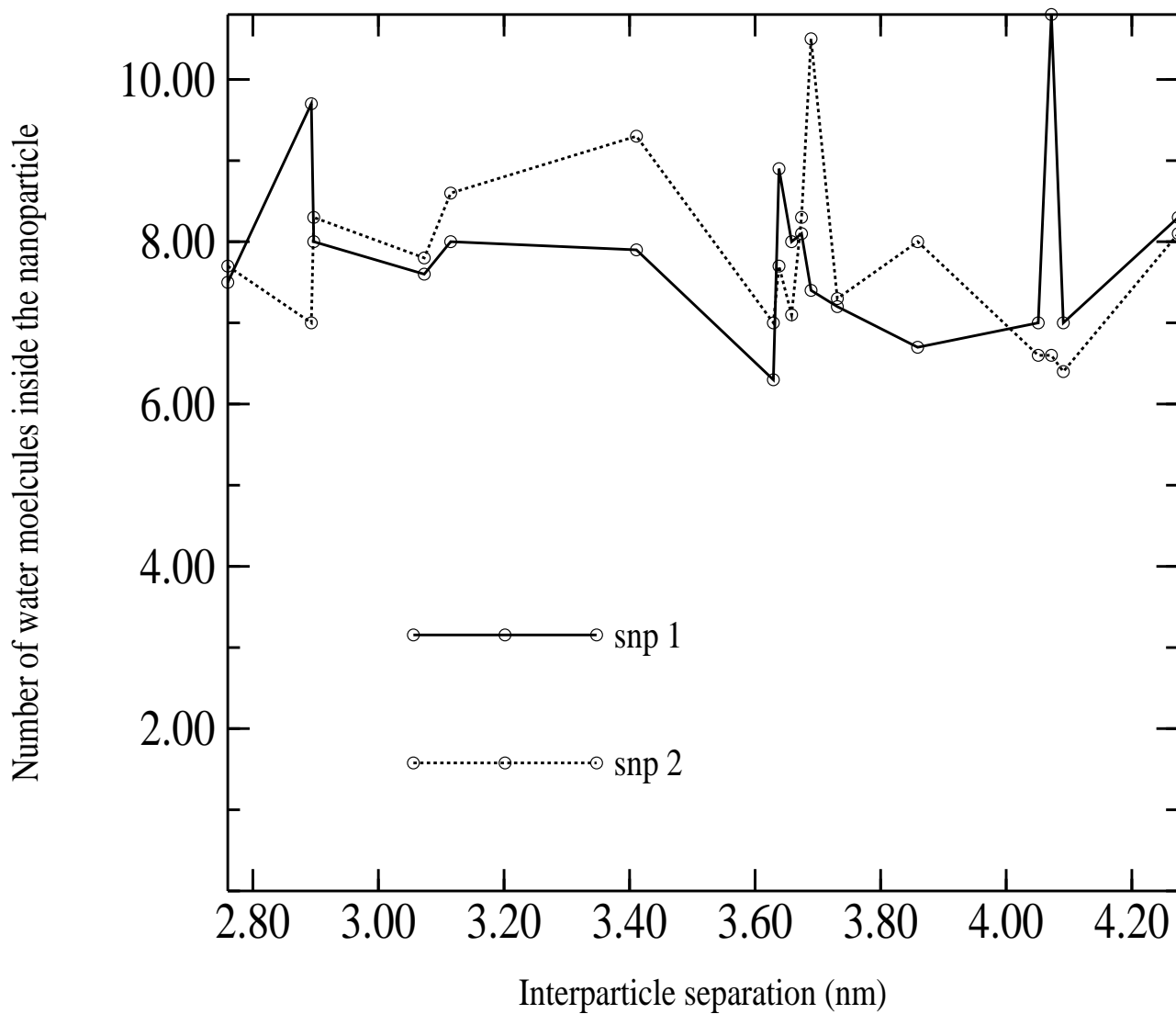




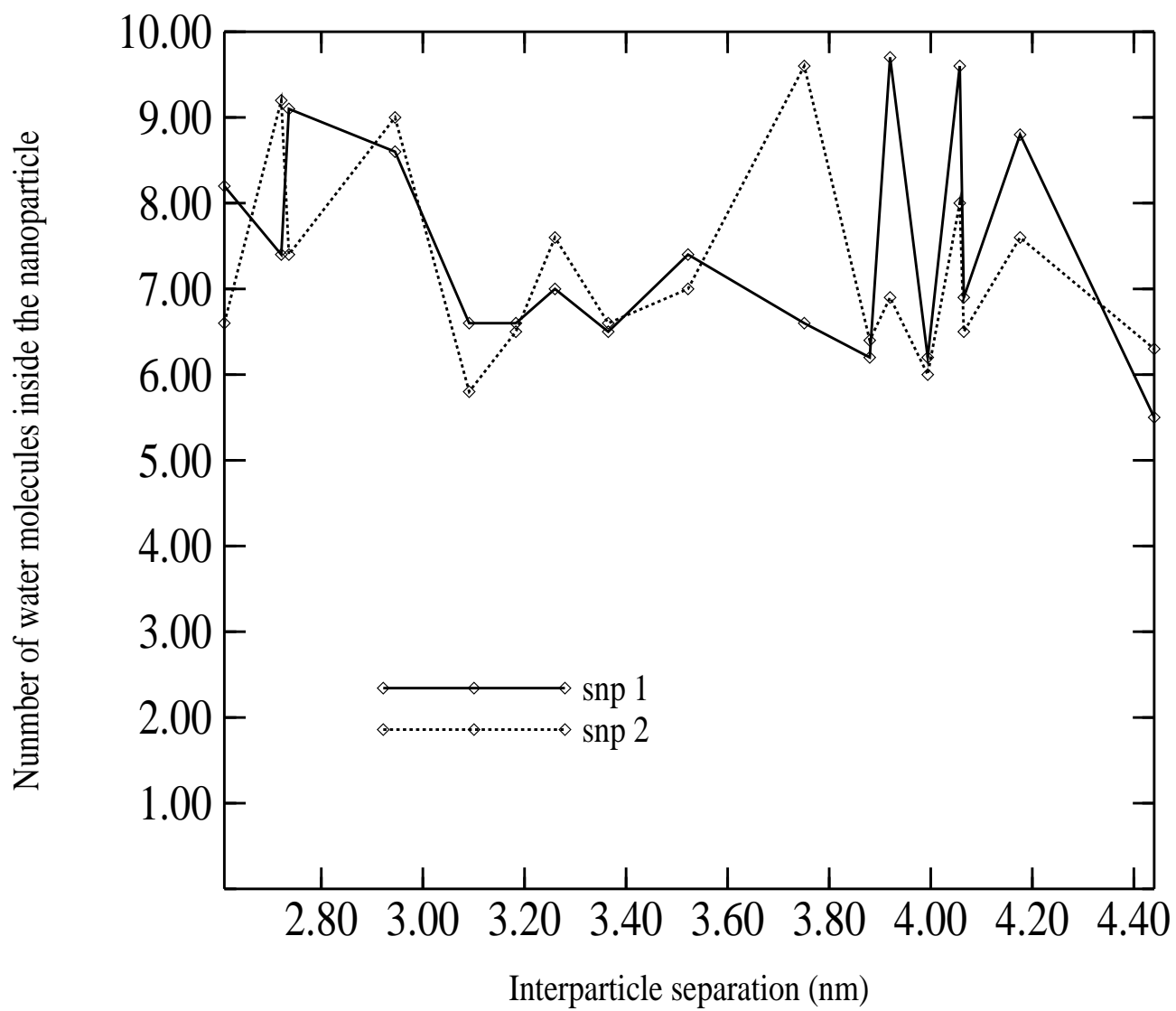
(a)



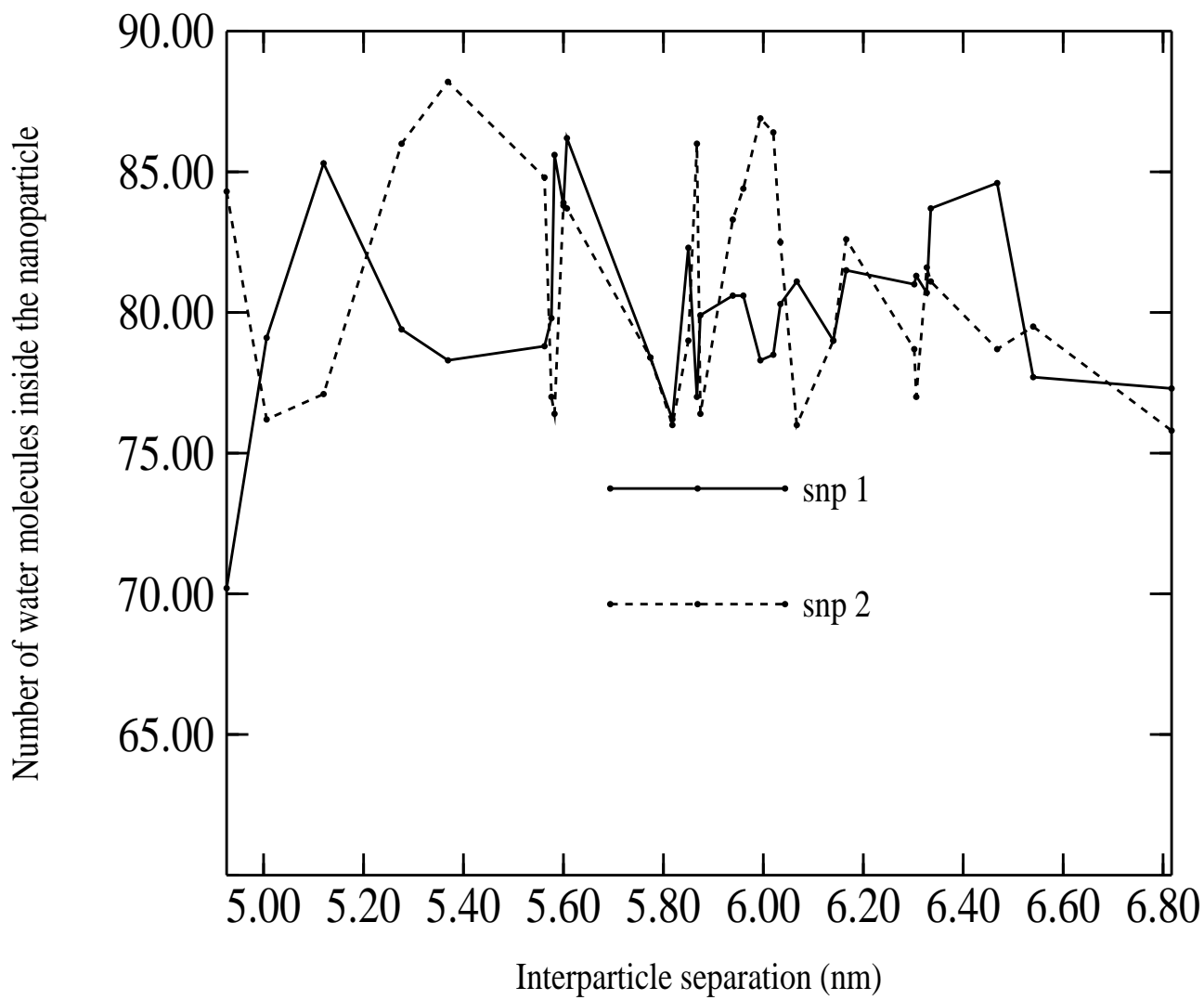
(b)



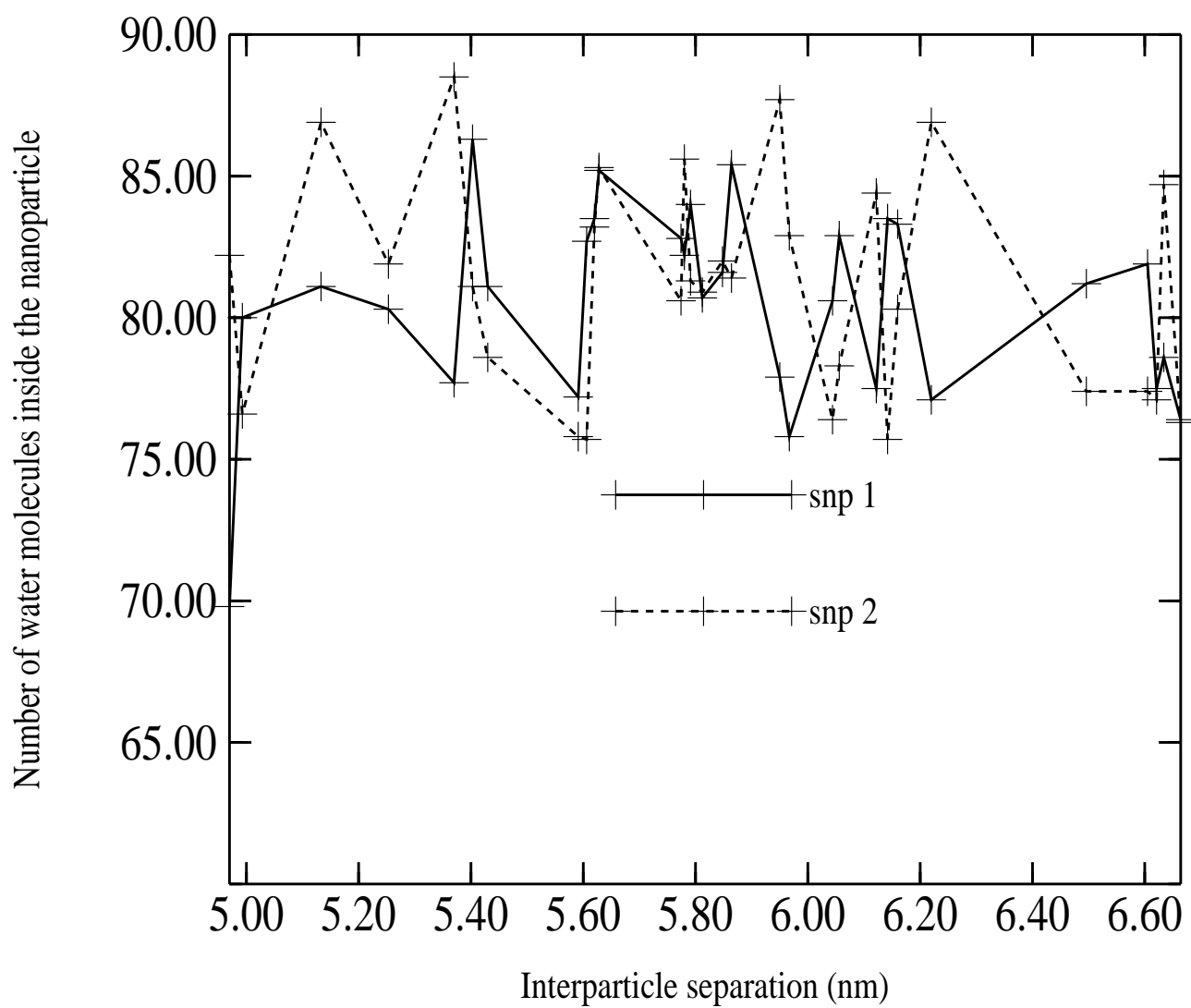
(c)



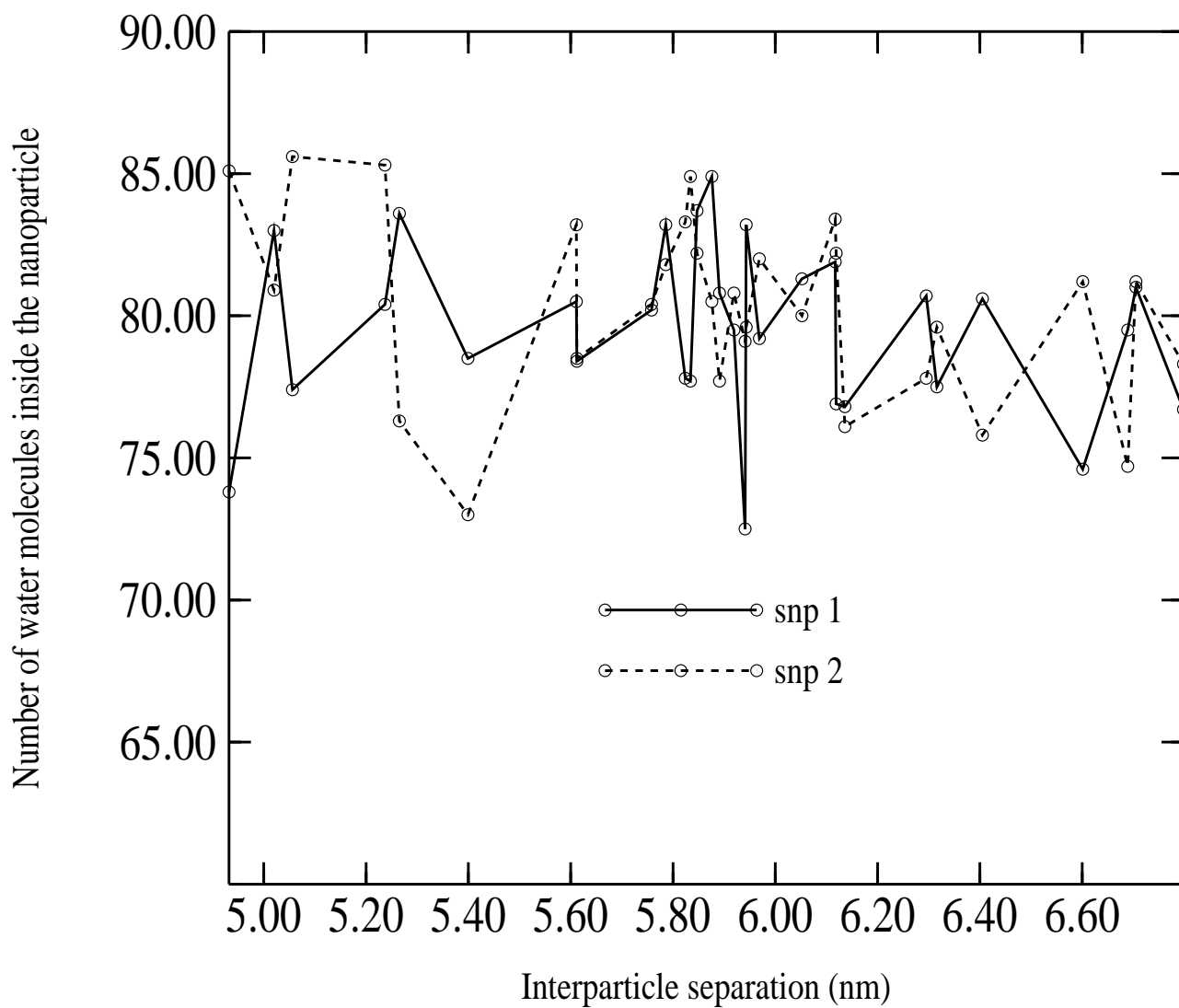
(d)



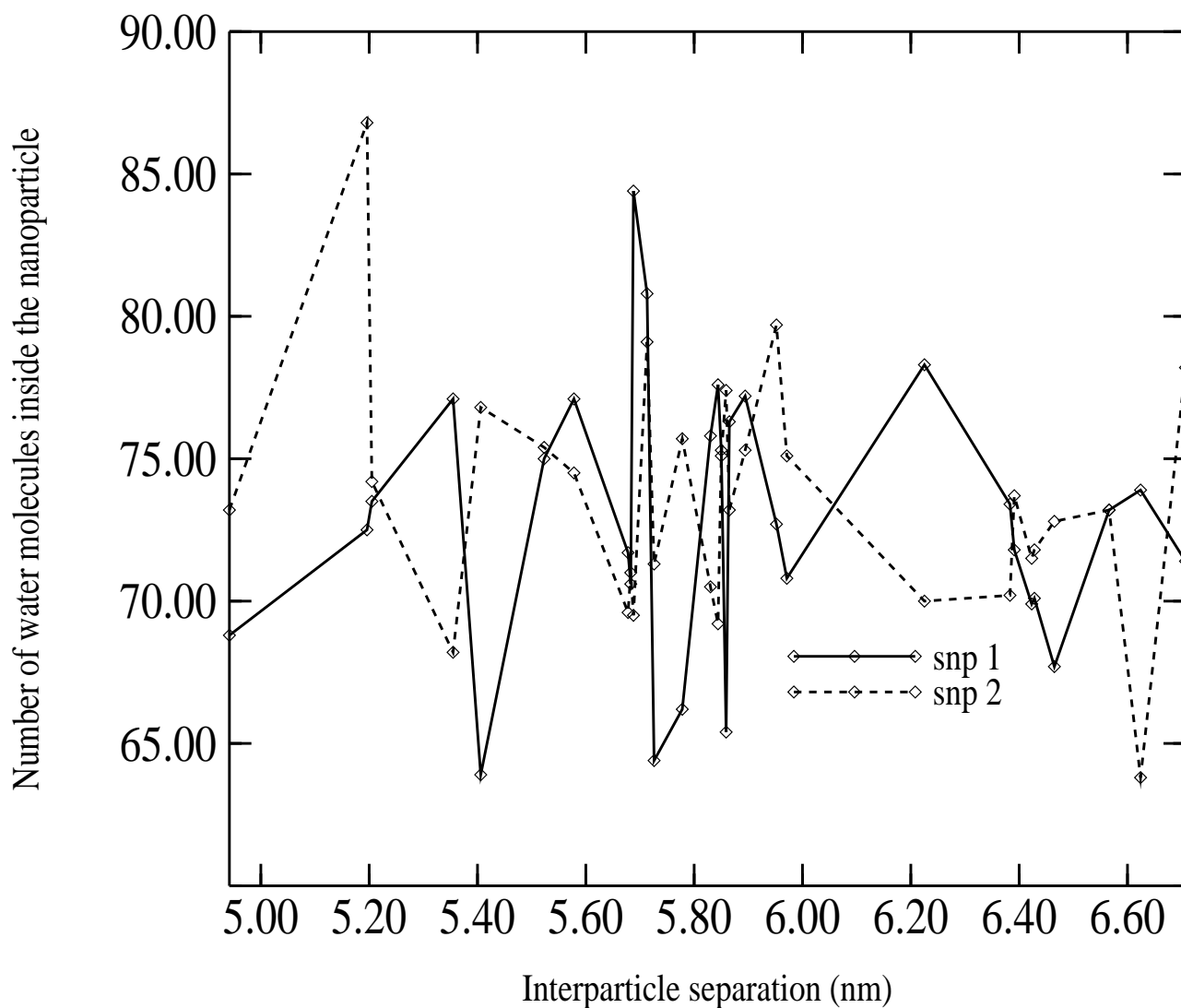
(e)



(f)



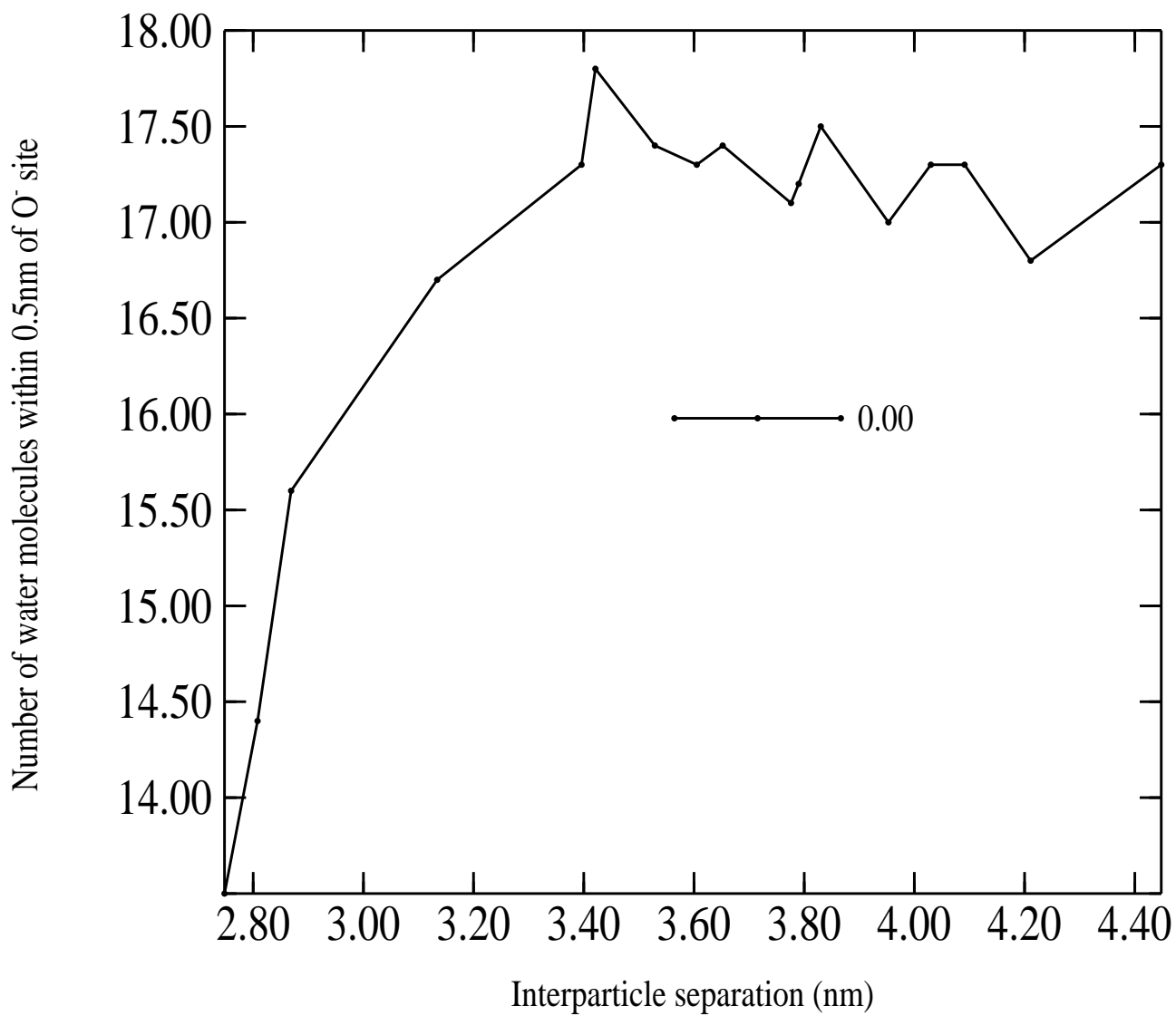
(c)



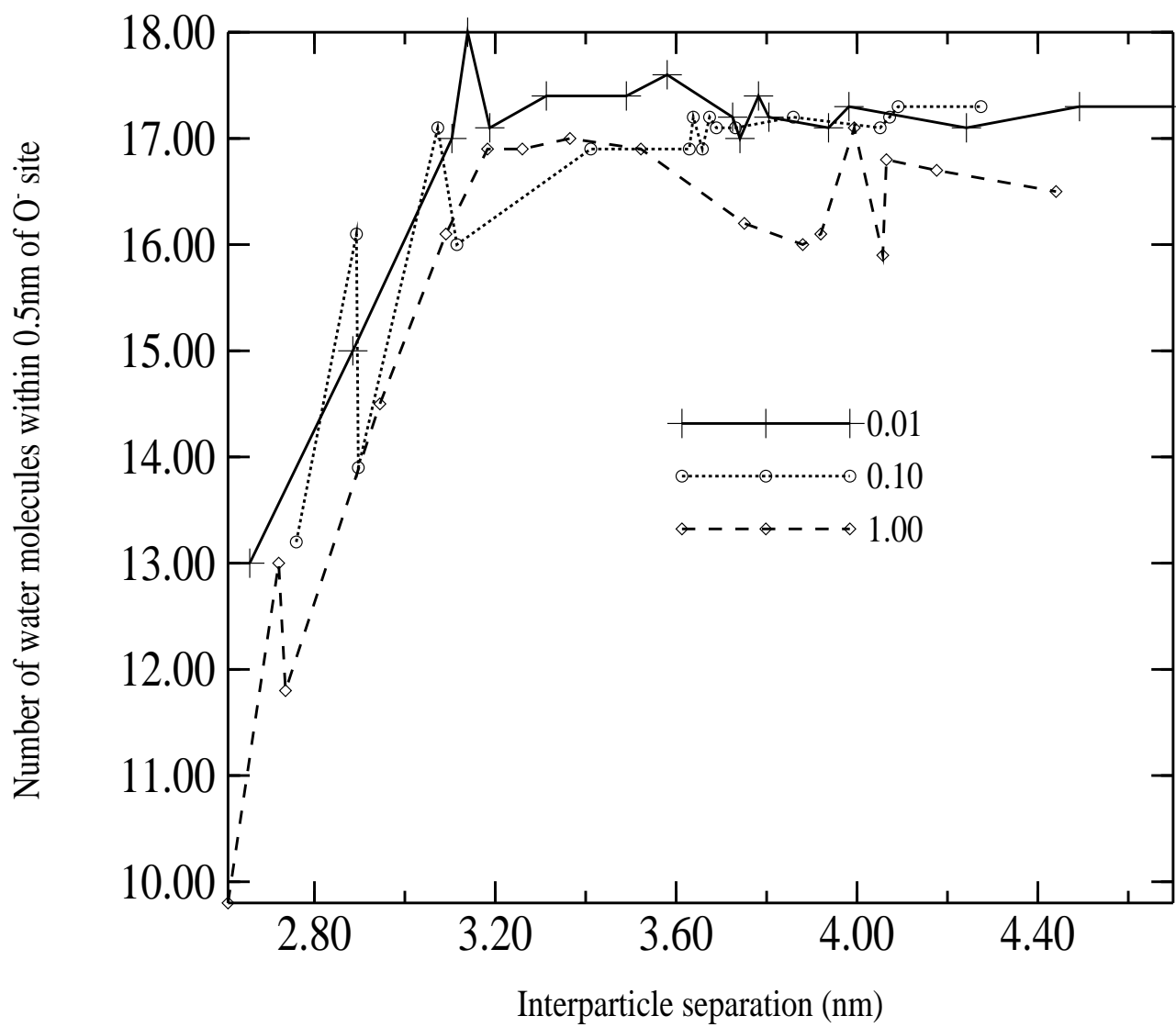
(h)

**Figure 4.** The plots for the silica nanoparticle with radius 2.0 nm showing the variation of the average number of the water molecules inside the specified radius, with background sodium concentration are shown in (a-d) (see Table 3). Plots (e-f) show the equivalent results for the silica nanoparticle with radius 4.4 nm (see Table 4) .

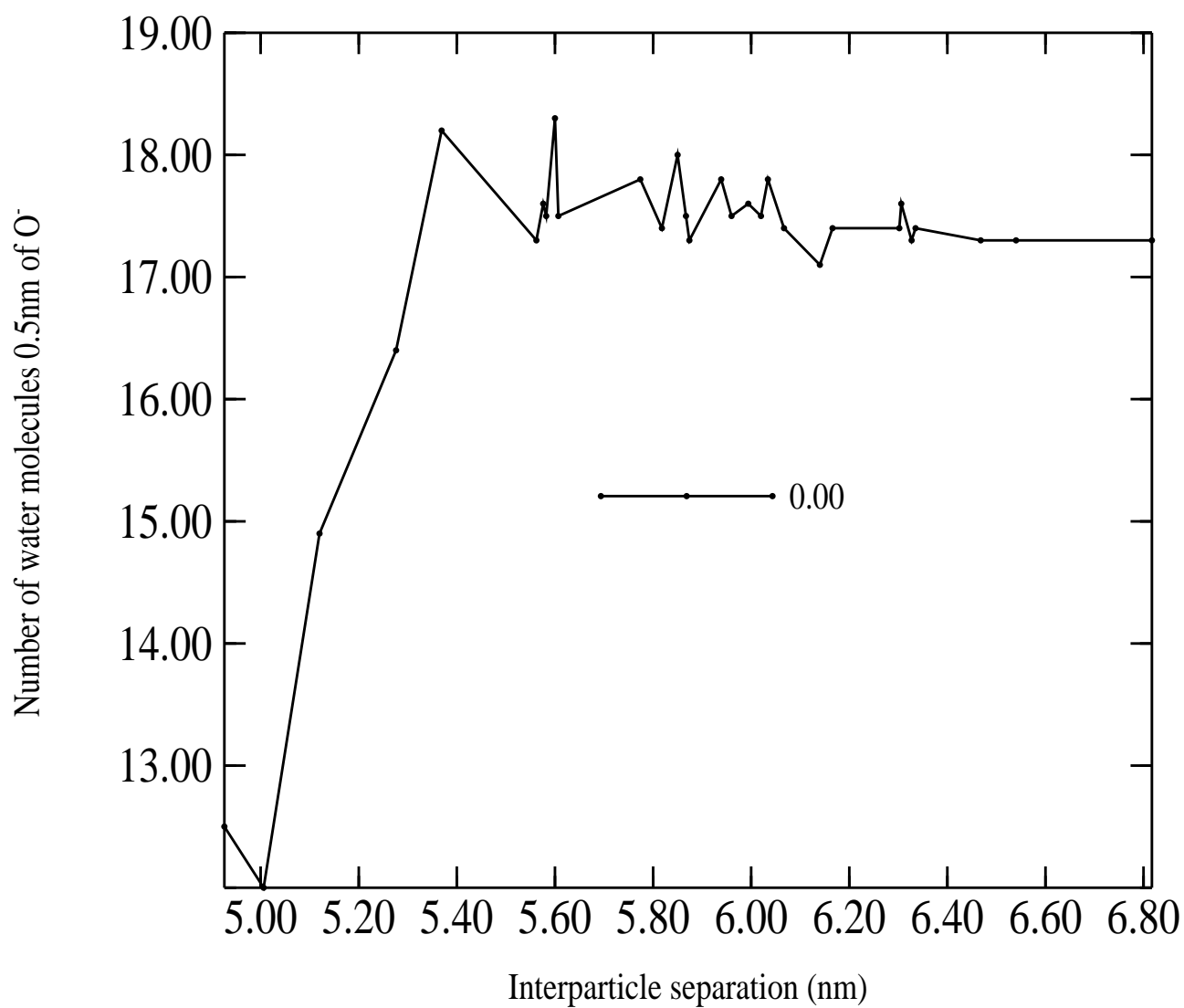




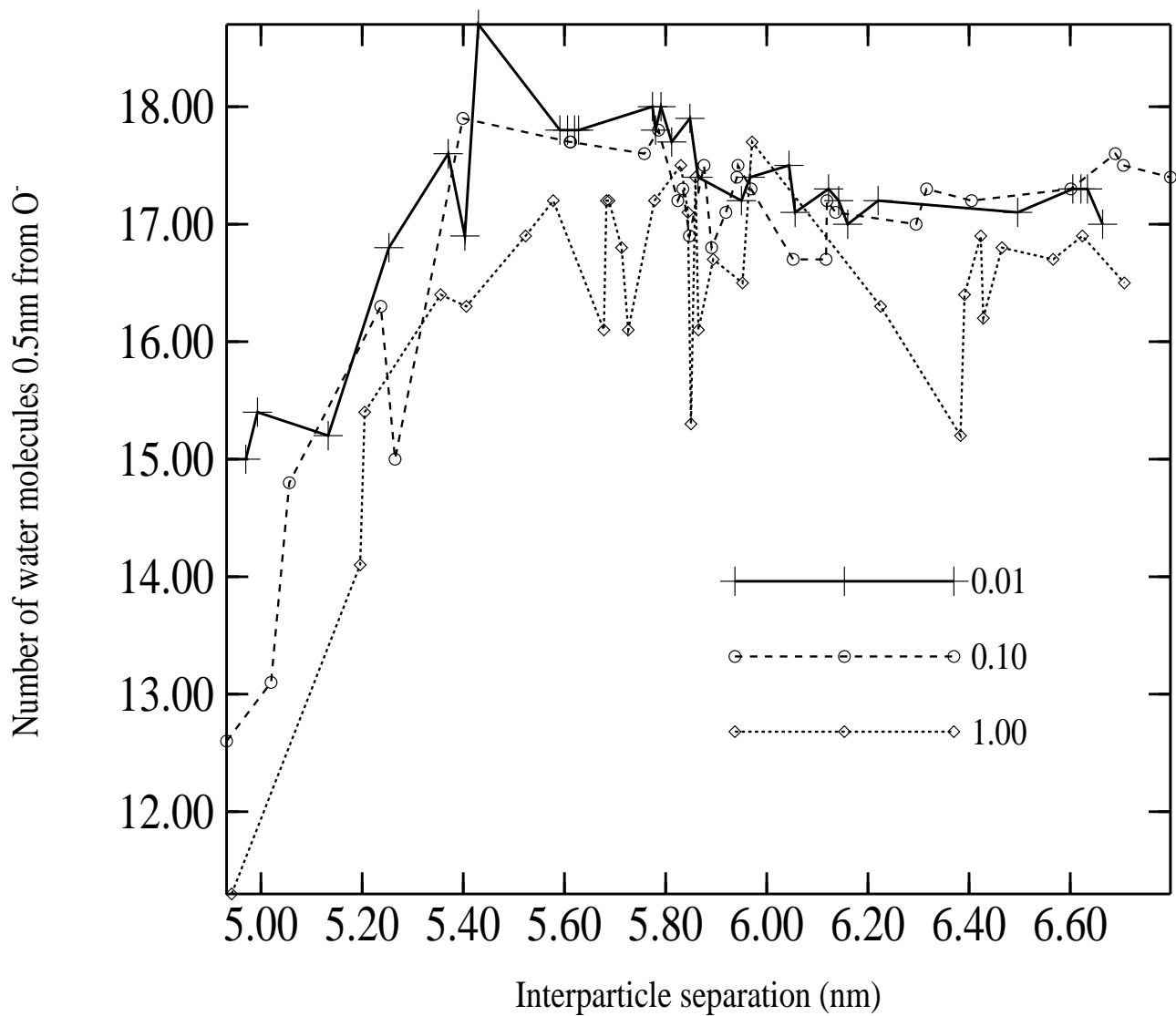
(a)



(b)

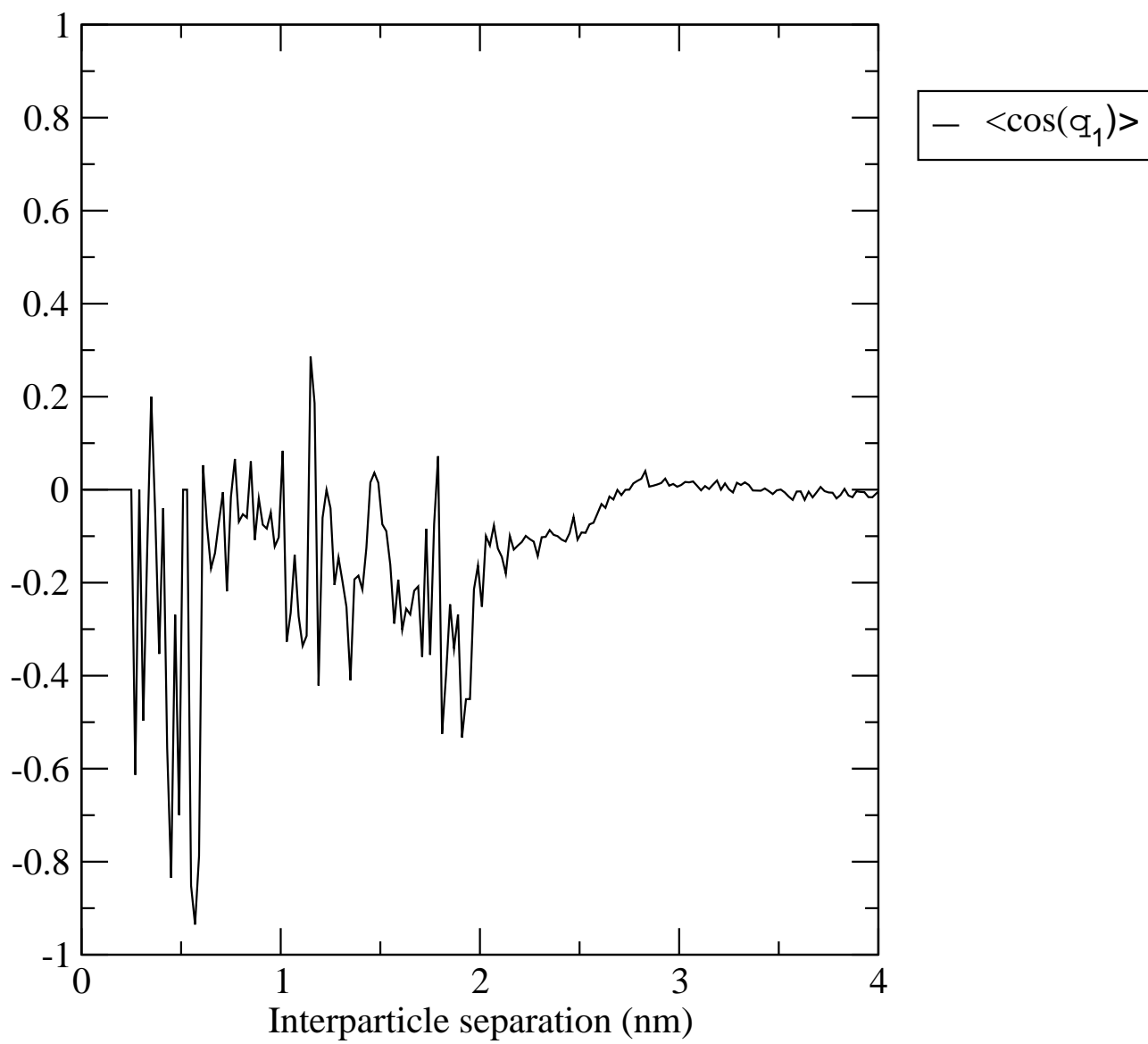


(c)

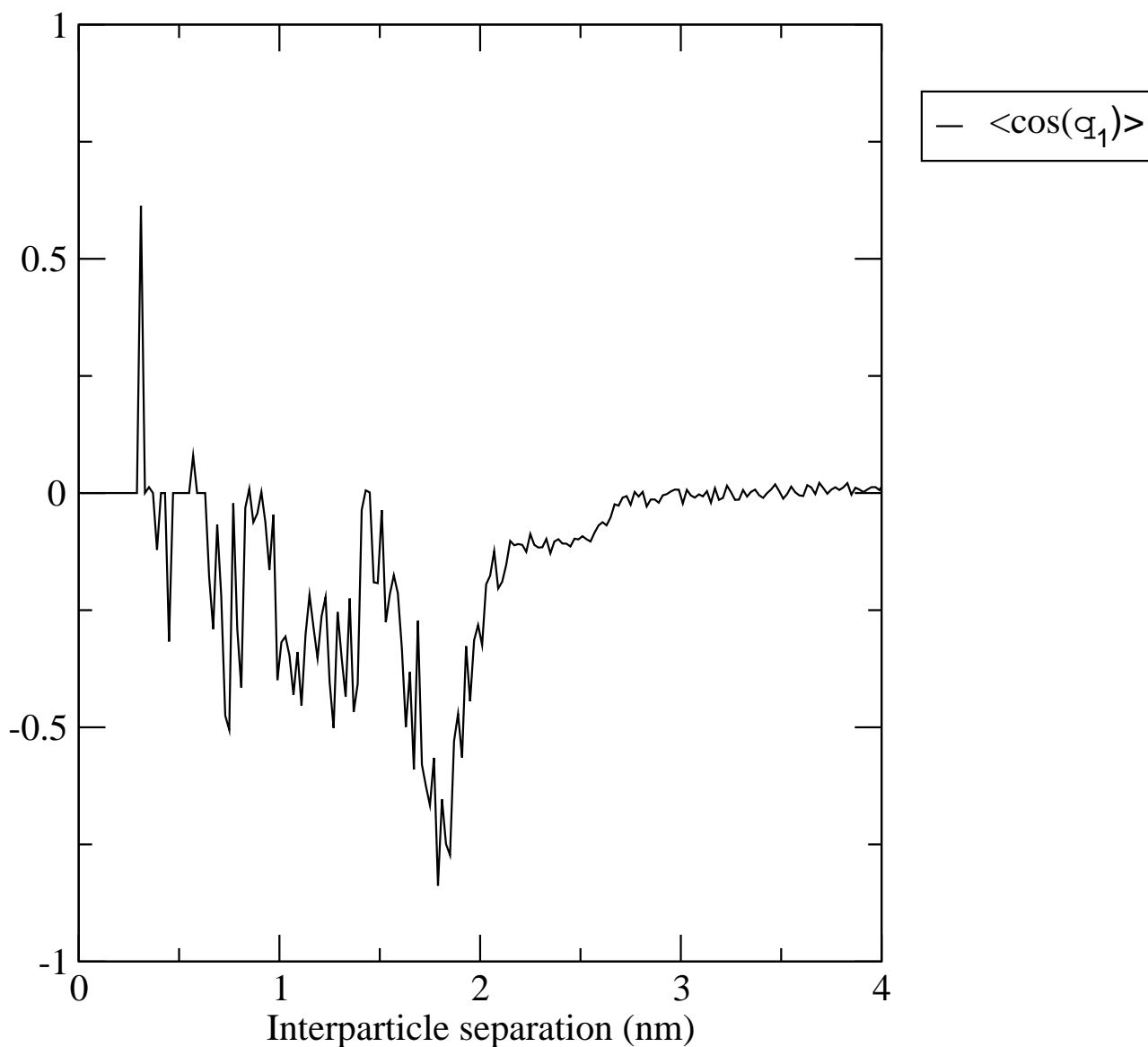


(d)

**Figure 5.** The variation of the time-averaged number of water molecules within a 0.5 nm radius of the O<sup>-</sup> deprotonated silanol surface sites. The individual nanoparticles are distinguishable within the figure, and labelled 'snp 1' and 'snp 2'. Results for the nanoparticle with diameter 2.0 nm are given in (a-b) and that of the nanoparticle with diameter 4.4 nm are shown in (c-d).

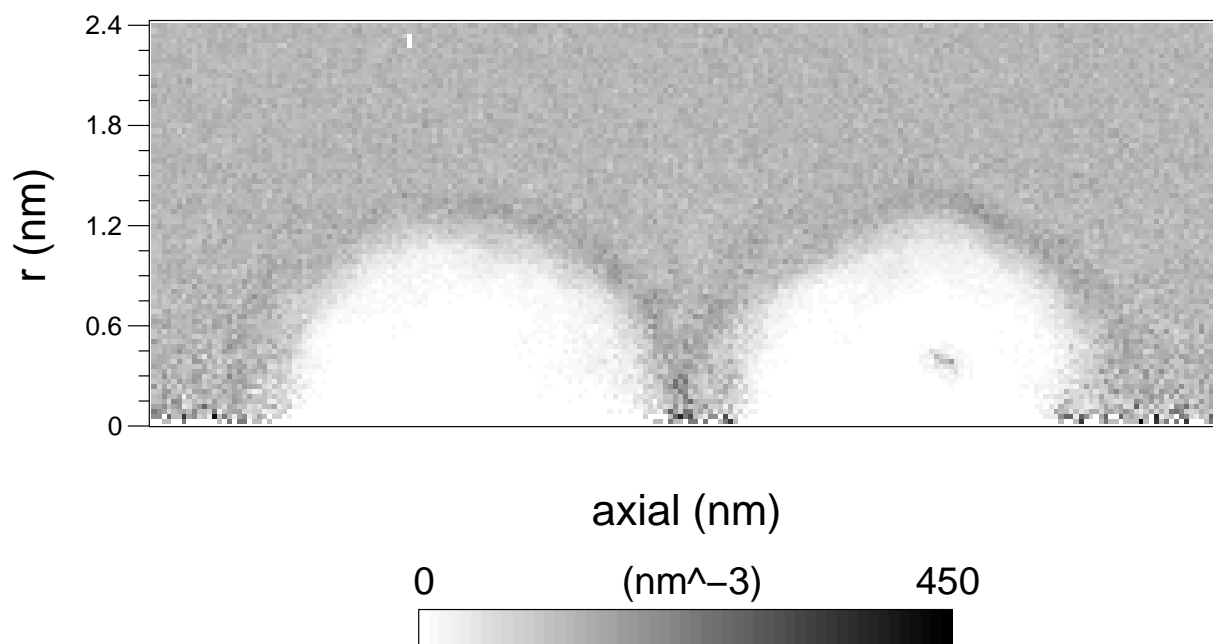


(a)

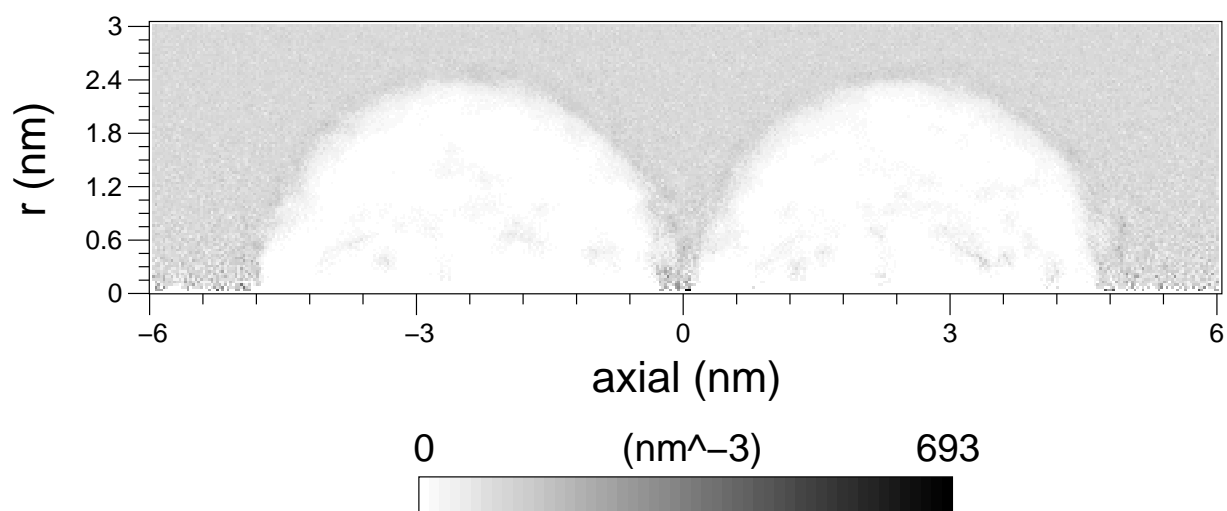


(b)

**Figure 6.** The time-averaged orientation of water molecules within the defined radius relative to the centre of mass of a silica nanoparticle shown for the isolated particle in (a) and for one particle from a pair in (b). The outer cutoff radius for the time-averaged water molecule orientation of the nanoparticle with diameter 2.0 nm is 1.0 nm and for the nanoparticle with diameter 4.4 nm the cutoff radius is 2.2 nm. A value of +1 or -1 for  $\cos(q_1)$  represents a water molecule oriented so that the bisecting in-plane vector (of the water molecule) is parallel or anti-parallel respectively to the vector joining the centre of mass of the nanoparticle to the oxygen atom of the water molecule. The impermeability is given (from the origin along the x-axis) as the maximum extent to which  $\langle \cos(q_1) \rangle = 0$  is true, see Tables 3 and 4.



(a)



(b)

**Figure 7.** The axial-radial density plots of the distributions of water molecules around the pair of nanoparticles for the entire MD trajectory is shown for the pair of nanoparticles with diameters 2.0 nm and 4.4 nm are shown in (a) and (b) respectively. The axis corresponds to the line joining the centres of mass of the two particles. NB, (a) is already in Part I of this work but is included here for ease of comparison with (b). Water is visible inside the nanoparticle in (b).

**Table 1.** Summary of the radial distribution function ratios for the silica nanoparticle(s) with diameter 2.0 nm. Each entry in the table is the ratio of the heights of the second to first peaks of the corresponding radial distribution function for each background sodium concentration given by the column heading (see also Figure 3).

RDF species	<b><u>RDF ratios</u></b>			
	Background sodium ion (Na <sup>+</sup> ) molarity			
	0.00	0.01	0.10	1.00
<b>Na<sup>+</sup> and H<sub>2</sub>O</b>				
<i>snp 1 + snp 2</i>	0.391	0.442	0.508	0.578
<i>isolated</i>	0.379	0.419	0.458	0.590
<b>O<sup>-</sup> and H<sub>2</sub>O</b>				
<i>snp 1 + snp 2</i>	0.401	0.440	0.451	0.450
<i>isolated</i>	0.417	0.430	0.447	0.413
<b>O<sup>-</sup> and Na<sup>+</sup></b>				
<i>snp 1 + snp 2</i>	0.127	0.091	0.082	0.135
<i>isolated</i>	0.101	0.127	0.074	0.194

**Table 2.** Summary of the radial distribution function ratios for silica nanoparticle(s) with diameter 4.4 nm. Each entry in the table is the ratio of the heights of the second to first peaks of the corresponding radial distribution function for each background sodium concentration given by the column heading.

RDF species	<b><u>RDF ratios</u></b>			
	Background sodium ion (Na <sup>+</sup> ) molarity			
	0.00	0.01	0.10	1.00
<b>Na<sup>+</sup> and H<sub>2</sub>O</b>				
<i>snp 1 + snp 2</i>	0.390	0.406	0.465	0.473
<i>isolated</i>	0.380	0.423	0.471	0.572
<b>O<sup>-</sup> and H<sub>2</sub>O</b>				
<i>snp 1 + snp 2</i>	0.440	0.446	0.448	0.427
<i>isolated</i>	0.462	0.453	0.441	0.463
<b>O<sup>-</sup> and Na<sup>+</sup></b>				
<i>snp 1 + snp 2</i>	0.047	0.040	0.050	0.061
<i>isolated</i>	0.061	0.038	0.049	0.063



**Table 3.** The mean of the time-averaged number of water molecules trapped inside nanoparticles with diameter 2.0 nm, (see also Figure 4(a-d)). The individual nanoparticles are distinguishable within the table and Figure 4, labelled 'snp 1' and 'snp 2' and 'isolated' refers to calculations performed on the isolated nanoparticle. The 'bare' particle refers to the case of the isolated particle with fully *protonated* silanol surface sites. The figures in brackets describe the mean of the time-averaged value of the impermeability of the nanoparticles given in nanometres; see Figure 6(a-b) and accompanying text.

**Mean of the time-averaged number of trapped water molecules and impermeability**

<b>Background sodium ion (Na<sup>+</sup>) molarity</b>				
<b>species</b>	<b>0.00</b>	<b>0.01</b>	<b>0.10</b>	<b>1.00</b>
<i>snp 1</i>	8.3 (0.447)	8.1 (0.511)	7.9 (0.506)	7.5 (0.453)
<i>snp 2</i>	7.9 (0.479)	7.8 (0.446)	7.8 (0.495)	7.2 (0.480)
<i>isolated</i>	7.4 (0.550)	6.9 (0.629)	6.9 (0.472)	5.9 (0.652)
<i>bare</i>	6.7 (0.451)	6.1 (0.310)	7.2 (0.291)	5.5 (0.310)

**Table 4.** The mean of the time-averaged number of water molecules trapped inside nanoparticles with diameter 4.4 nm, (see also Figure 4(e-h)). See also the accompanying text for Table 3.

**Mean of the time-averaged number of trapped water molecules and impermeability**

<b>Background sodium ion (Na<sup>+</sup>) molarity</b>				
<b>species</b>	<b>0.00</b>	<b>0.01</b>	<b>0.10</b>	<b>1.00</b>
<i>snp 1</i>	80.2 (0.468)	80.5 (0.443)	79.5 (0.437)	72.9 (0.475)
<i>snp 2</i>	80.9 (0.374)	81.1 (0.354)	80.4 (0.379)	73.5 (0.347)
<i>isolated</i>	92.1 (0.252)	94.7 (0.292)	93.3 (0.290)	85.5 (0.253)